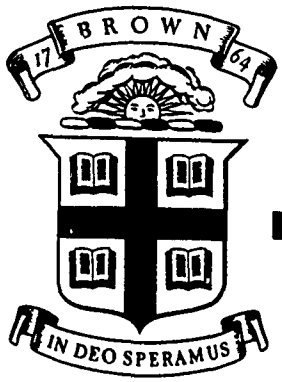

Brown University
DIVISION OF ENGINEERING
PROVIDENCE, R.I. 02912

Simulation of Transient Glide of a Threading Dislocation in an Embedded Strained Expitaxial Layer

Jean-Claude Ramirez*, Allan Bower**, and L. B. Freund

Division of Engineeering
Brown University
Providence, Rhode Island 02912

Simulation of Transient Glide of a Threading Dislocation in an Embedded Strained Expitaxial Layer

Jean-Claude Ramirez*, Allan Bower**, and L. B. Freund

Division of Engineeering
Brown University
Providence, Rhode Island 02912

Office of Naval Research
Contract N00014-87-K-0481

National Science Foundation
Grant DMR 87-14665

IBM Corporation
Research Award in Materials Science

July 1990

*Presently at Hibbitt, Karlsson, and Sorensen Inc., Providence, RI.
**Presently at Department of Engineering, University of Cambridge, Cambridge, UK.

Simulation of Transient Glide of a Threading Dislocation in an Embedded Strained Epitaxial Layer

by

Jean-Claude Ramirez*, Allan Bower**, and L. B. Freund

Division of Engineering, Brown University
Providence, R.I. 02912

Abstract

The material configuration considered is a thin strained layer embedded between two relatively thick, unstrained layers. The interfaces between the strained layer and the unstrained layers are assumed to be epitaxial, and the strain in the layer is assumed to arise from a mismatch in lattice parameters between the strained layer material and the surrounding material. For purposes of calculation, the crystalline materials are assumed to have cubic symmetry, oriented so that the [001] direction is normal to the interfaces. Initially, a long straight 60° dislocation exists on a {111} plane, extending from one otherwise strain-free region, through the strained layer, and into the other strain-free region. The purpose here is to model the process of glide of this dislocation under the action of the stress associated with the mismatch strain in the layer. The shape of the dislocation during glide is approximated by a continuous piecewise linear curve, and the location of the vertices of this curve are viewed as generalized coordinates of the system. A corresponding generalized force is defined at each node as the variation in total energy of the system due to variation in position of that node. A kinetic law of motion, suitable for thermally activated glide of the dislocation, is then cast into a form involving the nodal velocities and the corresponding generalized forces. The governing equations have been integrated numerically for material parameters representative of the GeSi/Si[001] strained layer systems. For layer thickness less than the critical thickness, the dislocation bows but its total motion is limited. On the other hand, when the layer thickness exceeds the critical thickness, glide reaches a steady state after the dislocation in the layer travels a distance only several times the layer thickness. Preliminary results are also reported for the situation when the gliding dislocation encounters an interface misfit dislocation in its path, the second dislocation having arrived at the interface through earlier glide on an intersecting glide plane.

* Presently at Hibbitt, Karlsson, and Sorensen Inc., Providence, R.I.
** Presently at Department of Engineering, University of Cambridge, Cambridge, U.K.

1. Introduction

Due to advances in the techniques of crystal growth over the past decade, it is possible to fabricate almost perfect bi-material crystals. If a thin layer of material is to be grown onto the plane surface of a second material of the same crystal structure and orientation, atoms can be deposited in such a way as to continue the crystalline structure of the substrate into the layer. Thus, the interface is coherent or epitaxial, at least in the early stages of growth. Furthermore, many layers can be deposited in sequence, creating a material with a periodic structure known as a 'superlattice'. A general introduction to this technology and its applications to electronics is given by Bean (1985). The growth processes are sophisticated, but are routinely performed by one of several techniques (for example, molecular beam epitaxy or organometallic vapor phase epitaxy) in many laboratories.

By proper selection of materials or alloys, it is possible to match the lattice spacing of the layer to that of the substrate. Two examples are the growth of AlGaAs on GaAs or $In_{0.53}Ga_{0.47}As$ on InP. In this case, the layer grows without intrinsic strain. These lattice matched structures have been important in the development of electronic and opto-electronic devices with desirable characteristics, typically high speed response, small size and low power consumption.

In the past few years, the prospect of epitaxial growth of a layer on a substrate in a situation where the lattice parameter of the layer differs from that of the substrate has attracted great interest. A modest amount of mismatch is accommodated by an extensional strain in the layer, so that the crystal lattice in the layer remains perfectly registered with that of the substrate. This process has come to be known as strained layer epitaxy. Not all of the effects of strain on the electronic structure of the material are known. However, it appears that the mechanical strain can be exploited to tailor the electronic energy band structure of the material for specific purposes. For example, strain can be used to separate multiple modes at a certain energy level, to convert an indirect band gap material to a direct band gap material, or to adjust the size of the energy gap between the highest bound states and the lowest conduction states of charge carriers in doped semiconductor materials.

A difficulty with manufacturing reliable strained layer structures is that the mismatch strain gives rise to a driving force for the nucleation and growth of defects in the strained layer lattice. Such defects usually degrade the electrical or optical performance of the material, so the means of controlling them has become a concern of central importance. A defect that has attracted particular attention is the threading dislocation in a strained layer. For a surface layer, this is a

slip dislocation with the dislocation line extending across the strained layer, and then continuing either along the interface or into the substrate. For an embedded layer, the line of the threading dislocation may continue along both interfaces or extend into adjacent material above and below the layer. This defect is important because it can move through the layer under the action of the internal stress, leaving behind segments of misfit dislocation in the interface. As the length of interfacial dislocation increases, the mismatch strain in the layer is progressively relaxed.

The concept of a critical layer thickness for the onset of strain relaxation has played a central role in studies of epitaxial layers (Matthews et al, 1970). There is a simple explanation for this phenomenon. Suppose that a dislocation extends from the free surface of the layer across its thickness, and continues along the interface as a misfit dislocation. If the layer thickness is less than a certain value h_c, the work necessary to form a length of misfit dislocation exceeds the energy released in relaxing the strain in the layer, so the threading dislocation does not tend to advance spontaneously. On the other hand, if the layer is thicker than h_c, the opposite is true and there is a driving force tending to advance the dislocation. The discriminating thickness is called the *critical thickness* of the layer. For a given uniform mismatch elastic strain in the layer, the threading dislocation will tend to move so as to reduce the length of interface misfit dislocation if the layer thickness is below the critical thickness h_c, whereas it will tend to increase the length of interface misfit if the layer thickness exceeds h_c.

One of the more fruitful extensions of this idea has been to estimate the spacing between dislocations in a partially relaxed layer at a given initial mismatch strain and layer thickness. This extension is based on the additional assumptions that the remaining elastic strain in the film is spatially uniform, and that there is a ready source of dislocations. However, dislocation densities observed experimentally are much lower than this calculation predicts. Several assumptions in the theory may not be satisfied in practice. For example, the model presumes the availability of a supply of threading dislocations whereas, in reality, dislocations must be nucleated, a process which is typically more difficult to activate than steady glide of a threading dislocation (Fitzgerald et al, 1989; Eaglesham et al, 1989; Tuppen et al, 1989). Dislocation mobility in semiconductor materials is low, so that the rate of elastic strain relaxation can also be limited by the kinetics of dislocation motion (Hull et al, 1988; Dodson and Tsao, 1987; Freund et al, 1989). Another possible impediment to the glide of threading dislocations is the interaction between dislocations on intersecting glide planes. For example, for the case of 350 Å $Ge_{0.25}Si_{0.75}$ layers on Si it has been reported that the lengths of individual interface dislocation lines did not increase significantly during relaxation, even

though the number of dislocations increased (Hull et al, 1989). Furthermore, the hesitation of a threading dislocation as it encounters a misfit dislocation in its path is evident in the real-time video recordings of threading dislocation motion in SiGe/Si films during an anneal (Hull and Bean, 1990). It was suggested that this behavior may be due to the interaction of dislocations on intersecting glide systems.

The purpose here is to examine the kinetics of glide of a threading dislocation in an embedded strained layer. The glide is assumed to be a thermally activated process appropriate for silicon, germanium and other covalent materials. Previous analyses of this process have been based on steady glide of a dislocation of fixed shape. In this work, the complete shape of the threading dislocation is calculated during both the early transient and steady state phases of its motion. The three-dimensional dislocation line is approximated by a series of straight segments, as discussed in section 2. The shape of the dislocation is determined by calculating the energetic driving force on each segment, and integrating the resulting kinetic equations, as discussed in sections 3 and 4. The results for glide of a single, isolated threading dislocation in an embedded strained layer are reported in section 5, and the interaction of this dislocation with a pre-existing dislocation on an intersecting glide plane is considered in section 6.

2. Description of the Model

Consider the embedded strained layer shown in Figure 1. A dislocation is assumed to glide on a particular plane (shaded in the figure). A rectangular x_1, x_2, x_3-coordinate system is introduced with origin in the midplane of the layer as shown. The unit vector $\mathbf{n}$ is the normal to the glide plane in the x_3-direction. Suppose that, in the absence of the gliding dislocation, an equilibrium stress field $\boldsymbol{\sigma}^A$ exists in the bimaterial composite. This field can be a spatially uniform isotropic membrane tension confined to the layer or a nonuniform stress distribution due to a dislocation on an intersecting glide plane. These two situations, for the case of a layer on a single substrate, have been recently considered in detail by Freund (1989).

It is assumed here that the dislocation tends to move so as to decrease the mechanical energy of the system. The elastic energy associated with any particular dislocation configuration is defined as the net work done in introducing the fully formed dislocation into the stressed body. If $\boldsymbol{\sigma}^D$ is the equilibrium stress field due to the dislocation in the absence of any applied loading and if $\boldsymbol{\sigma}^A$ is the applied stress field, the energy is

$$E(S) = \frac{1}{2}\int_S \mathbf{b}\cdot(\boldsymbol{\sigma}^D\cdot\mathbf{n})\,dS + \int_S \mathbf{b}\cdot(\boldsymbol{\sigma}^A\cdot\mathbf{n})\,dS, \tag{2.1}$$

where S is the slipped area with unit normal $\mathbf{n}$ and $\mathbf{b}$ is the Burgers displacement vector of the dislocation. For a glide dislocation $\mathbf{b} \cdot \mathbf{n} = 0$. The boundary of the slipped area in the glide plane is denoted by B, and the outward normal to B in the plane is $\mathbf{m}$. The stress field σ^D is sometimes called the self-stress of the dislocation.

By applying Blin's formula (Hirth and Lothe, 1982) for the energy of interaction between two dislocation loops, the first integral in (2.1) can be expressed in terms of line integrals over the boundary B of the slipped area, resulting in the following expression for the energy of the system:

$$E(S) = \frac{\mu}{8\pi} \oint_B \oint_B \frac{(\mathbf{b} \cdot d\mathbf{l}_1)(\mathbf{b} \cdot d\mathbf{l}_2)}{R} + \frac{\mu}{8\pi(1-\nu)} \oint_B \oint_B (\mathbf{b} \times d\mathbf{l}_1) \cdot \mathbf{T} \cdot (\mathbf{b} \times d\mathbf{l}_2) + \int_S \mathbf{b} \cdot (\sigma^A \cdot \mathbf{n})\, dS \qquad (2.2)$$

where R is the separation distance between the differential line elements $d\mathbf{l}_1$ and $d\mathbf{l}_2$, and $\mathbf{T}$ is a tensor with rectangular components $\mathrm{T}_{ij} = \partial^2 R / \partial x_i \partial x_j$.

The purpose of this section is to describe a numerical method, based on some implications of (2.2), for analyzing the change in shape of a threading dislocation. For purposes of numerical simulation, the dislocation configuration of Figure 1 is approximated by a continuous, piecewise linear configuration. The energy of the system can then be expressed in terms of the positions of the vertices of the piecewise linear dislocation. Suppose that this approximation consists of a finite number of straight dislocation segments labeled C_i, $i = 0, \ldots, N+1$, each with the same Burgers vector $\mathbf{b}$. The slipped area of this configuration is denoted by $\bar{S}$ and its boundary by $\bar{B}$. The approximate configuration is then fully described by the endpoints of these segments. Perhaps the simplest description of the configuration is illustrated in Figure 2. It consists of $N+1$ nodes, N straight segments C_i of variable (but finite) length L_i, and two "infinite" segments C_0 and C_{N+1}. A single generalized coordinate a_i is associated with each node, and it is a measure of the distance of the node in the x_2-direction from a datum parallel to the x_1-axis. Nodes are constrained against motion in the x_1-direction. The so-called infinite segments are necessary in order to properly model an arbitrarily long threading dislocation, but they are unnecessary when modelling any finite configuration.

For the case of a piecewise linear dislocation configuration, the integrals in (2.2) must be evaluated around $\bar{B}$, the boundary of the approximate configuration. This leads to the discretization of the integrals in (2.2)

$$E(\bar{S}) = \frac{\mu}{16\pi} \sum_{i=0}^{N+1} \sum_{m=0}^{N+1} \int_{C_i} \int_{C_m} \frac{(\mathbf{b} \cdot d\mathbf{l}_1)(\mathbf{b} \cdot d\mathbf{l}_2)}{R} +$$

$$\frac{\mu}{16\pi(1-\nu)}\sum_{i=0}^{N+1}\sum_{m=0}^{N+1}\int_{C_i}\int_{C_m}(\mathbf{b}\times d\mathbf{l}_1)\cdot\mathbf{T}\cdot(\mathbf{b}\times d\mathbf{l}_2)+\int_{\bar{S}}\mathbf{b}\cdot(\sigma^A\cdot\mathbf{n})\,dS. \qquad (2.3)$$

The explicit expressions for the integrals in (2.3) will be addressed in the next section.

The variation of energy with a local change in the shape of the dislocation line may be thought of as a force tending to distort the dislocation. The force is defined as the negative gradient of the of the interaction energy with respect to the position of the dislocation. Since the approximate configuration is characterized by generalized corner coordinates a_i, it is natural to introduce the generalized nodal force

$$G_i = -\frac{\partial E(\bar{S})}{\partial a_i}. \qquad (2.4)$$

The generalized force G_i is work-conjugate to a_i and acts in the direction of the displacement a_i. The notion of a generalized force on a dislocation serves as a convenient device for describing changes in its interaction energy and has been exploited in the elastic continuum theory of dislocations (see Dundurs (1969)). For instance, a dislocation configuration is said to be in equilibrium when its configurational energy is stationary or, in other words, when the force on the dislocation vanishes pointwise along the dislocation line. In this investigation, the force is used to calculate the rate of change of the corresponding coordinate a_i in order to study glide as a kinetic process.

According to Alexander (1986), the process of glide in covalent crystals, such as germanium and silicon, is a thermally activated, and the normal velocity $v^{(m)}$ of the dislocation line is given by a rate law of the form

$$v^{(m)} = V_o e^{-Q(\tau)/kT}, \qquad (2.5)$$

where V_o is a material constant with dimensions of speed, τ is the resolved shear stress in the direction of the Burgers vector on the glide plane, $Q(\tau)$ is the stress dependent activation energy for glide, k is Boltzman's constant, and T is absolute temperature. The notation $v^{(m)} = \mathbf{v}\cdot\mathbf{m}$ is intended to make clear the connection between the dislocation velocity $\mathbf{v}$ and the normal $\mathbf{m}$ to the boundary B of S. A particular form of the stress dependence of the activation energy in covalent crystals has been proposed by Alexander (1986) as

$$Q(\tau) = Q_o - E_o\log(\tau/\mu), \qquad (2.6)$$

where Q_o and E_o are material constants. Values of V_o, Q_o, and E_o for GeSi alloys based on an elementary mixture relation have been given by Freund (1989), and these values will be used in

section 5. At this point, it should be noted that the factor E_o/kT is of order unity for the materials being discussed here, and it is assumed hereafter that $E_o/kT = 1$.

The form of a rate law for glide of the discretized dislocation configuration in the a_i-direction at speed v_i, corresponding to (2.5), should have the feature that the nodal speeds v_i depend on the nodal forces G_i in the same way that v depends on τ in (2.5). A local kinetic equation relating v_i to G_i and having these properties is

$$v_i = v_o(i)e^{-Q(G_i/\mu bh)/kT} \tag{2.7}$$

where the multiplying factor $v_o(i)$ for each node is unknown. The factors $v_o(i)$ are determined by requiring that the energies dissipated through dislocation glide according to the discrete and continuum descriptions are identical, that is,

$$\int_B v^{(m)}(\ell)F(\ell)\,d\ell = \sum_i v_i\,G_i, \tag{2.8}$$

where $\bar{B}$ is the boundary of $\bar{S}$, and $F(\ell)$ is the so-called Peach-Koehler force per unit length on the dislocation line in the direction normal to the dislocation line. The Peach-Koehler force is given by $\mathbf{F} = (\mathbf{b}\cdot\boldsymbol{\sigma})\times\boldsymbol{\xi}$, where $\boldsymbol{\xi}$ a unit tangent to and in the direction of the dislocation (Dundurs (1969)). Thus, (2.8) can be rewritten in the more useful form

$$\int_B b\,v^{(m)}(\ell)\tau(\ell)\,d\ell = \sum_i v_i\,G_i. \tag{2.9}$$

Equation (2.9) enforces the notion that the generalized nodal forces G_i that drive the glide of the threading dislocation are the forces that are work rate-conjugate to the the kinematic rates v_i with respect to the time rate of change of the interaction energy $E(\bar{S})$.

To illustrate the ideas presented above, consider the dislocation configuration shown in Figure 3. This simplest of piecewise-linear configurations consists of five segments, C_0 through C_4, and four nodes, a_0 through a_3, and it is intended to approximate the threading dislocation of Figure 1 gliding down the embedded layer. The segments C_0 and C_4 are semi-infinite straight dislocations that extend indefinitely away from the embedded layer. The segments C_1 and C_3 model the misfit dislocations that are laid down along the bi-material interfaces as the dislocation segment C_2 is driven down the embedded layer. The glide plane of the dislocation is inclined at an angle α from the normal to the bi-material interface. The elastic mismatch strain in the layer is assumed to be an isotropic extensional strain ϵ_o in all directions parallel to the interface.

To simplify the analysis, assume that the two nodes a_0 and a_3 remain fixed and that the two inner nodes a_1 and a_2 are constrained to move together as one. The only degree of freedom in this problem is the position a of the center segment. The length L of this segment is the projected layer thickness $h/\cos\alpha$. It can be shown that the change in energy associated with the self-stress of the dislocation due to formation of the bow is

$$\begin{aligned}\Delta E_{\text{dislocation}} = &\frac{\mu}{2\pi}\left[b_1^2 + \frac{b_2^2}{1-\nu}\right]\left[\sqrt{L^2+a^2} - L - a + L\log\left(\frac{2L}{L+\sqrt{L^2+a^2}}\right)\right] \\ &- \frac{\mu}{2\pi}\left[b_2^2 + \frac{b_1^2}{1-\nu}\right]\left[L - \sqrt{L^2+a^2} + a\log\left(\frac{a+\sqrt{L^2+a^2}}{L}\right)\right] \\ &+ \frac{\mu}{2\pi}\left[b_2^2 + \frac{b_1^2}{1-\nu}\right] a\left[\log\left(\frac{a}{\rho}\right) - 1\right], \end{aligned} \tag{2.11}$$

where ρ is the core cutoff parameter. Likewise, it can be shown that the contribution to the change in energy due to the stress σ_o induced by the strain mismatch ϵ_o is

$$\Delta E_\sigma = -2\mu\frac{(1+\nu)}{(1-\nu)} aLb_1\epsilon_o \sin\alpha\cos\alpha. \tag{2.12}$$

The generalized nodal force G on the dislocation can be found as $-\partial\Delta E/\partial a$ according to (2.4), which leads to

$$\begin{aligned} G = &\frac{\mu}{2\pi}\left[b_1^2 + \frac{b_2^2}{1-\nu}\right]\left[1 - \frac{a}{L+\sqrt{L^2+a^2}}\right] - \frac{\mu}{2\pi}\left[b_2^2 + \frac{b_1^2}{1-\nu}\right]\log\left(\frac{aL}{\rho[a+\sqrt{L^2+a^2}]}\right) \\ &+ 2\mu\frac{(1+\nu)}{(1-\nu)} Lb_1\epsilon_o \sin\alpha\cos\alpha. \end{aligned} \tag{2.13}$$

A critical thickness condition for this approximate dislocation configuration is obtained from (2.13) by requiring that $G \to 0$ as $a \to \infty$. After some elementary manipulations, it is found that the critical layer thickness h_c for stability of the threading dislocation is given by

$$\epsilon_o = \frac{1}{4\pi(1+\nu)h_c \sin\alpha b_1}[b_1^2 + (1-\nu)b_2^2]\log\left(\frac{h_c}{2\rho\cos\alpha}\right). \tag{2.14}$$

This result is essentially the critical thickness of Matthews et al (1970).

In light of (2.14) the steady-state driving force G_{st} on the dislocation for layer thicknesses exceeding the critical thickness can be expressed as

$$G_{st} = \frac{\mu}{2\pi}\left[b_2^2 + \frac{b_1^2}{1-\nu}\right]\left[\left(\frac{h}{h_c}\right)\log\left(\frac{h_c}{2\rho\cos\alpha}\right) - \log\left(\frac{h}{2\rho\cos\alpha}\right)\right], \tag{2.15}$$

Alternatively, this driving force can be cast as an effective resolved shear stress (Tsao and Dodson, 1988)

$$\tau_{\text{eff}} = \frac{G_{st}}{b_1(h/\cos\alpha)} = \left\{1 - \left(\frac{h_c}{h}\right)\frac{\log(h/2\rho\cos\alpha)}{\log(h_c/2\rho\cos\alpha)}\right\}\sigma_o \sin\alpha\cos\alpha. \tag{2.16}$$

In this last expression, the effective resolved shear stress appears to be linear in σ_o. However, this is not the case because the critical layer thickness h_c is a function of the layer stress through the critical layer thickness criterion (2.14).

Using equations (2.5) and (2.7) in conjunction with equation (2.9) yields

$$\sum_{i=0}^{4}\int_{C_i}\left[v^{(m_i)}(\ell)\right]^2 d\ell = V_o h \sum_{i=0}^{3}\frac{v_i^2}{v_o(i)}, \tag{2.17}$$

where $v^{(m_i)}$ is the normal velocity of the segment C_i. For this configuration, the only nonzero normal velocity is that of segment C_2 and it is given by $v(a) = v_1 = v_2$, the velocity of nodes a_1 and a_2. Therefore, (2.17) simplifies to

$$\int_0^{h/\cos\alpha} v^2(a)\, d\ell = 2V_o h\,\frac{v^2(a)}{v_o(2)}, \tag{2.18}$$

from which it follows that

$$v_o(2) = 2\,V_o\cos\alpha. \tag{2.19}$$

The velocity of the dislocation is therefore

$$v(a) = 2V_o\left[\frac{G}{\mu b(h/\cos\alpha)}\right]e^{-Q_o/kT}, \tag{2.20}$$

where G is given in (2.13). This velocity reveals, among other things, the rate at which the threading dislocation lays down the two misfits of length a. If $h = h_c$ the velocity is zero. For $h > h_c$, the steady state velocity at which the glide dislocation lays down the interfacial misfits is obtained from (2.20) by setting $G = G_{st}$ in (2.20). In terms of the effective resolved shear stress derived earlier, the steady state velocity is given by

$$v_{st} = \frac{2V_o b_1}{\sqrt{(b_1^2 + b_2^2)}}\left(\frac{\tau_{\text{eff}}}{\mu}\right)e^{-Q_o/kT}. \tag{2.21}$$

It is straightforward to extend this procedure to a dislocation line with an arbitrary number of degrees of freedom. This issue is addressed below.

3. The Nodal Driving Forces

In this section, explicit expressions for the rate of change of the elastic energy of the dislocation with respect to variations in the positions of the nodes are obtained. The basis for this development is found in the expressions for the dislocation energy of two straight dislocation segments (Hirth and Lothe, 1982). These expressions are explicit equations for the first two integrals in (2.3), and they are different depending on whether the dislocation segments C_i and C_m are such that $i \neq m$ or $i = m$. These results are summarized next.

With attention restricted to planar configurations, consider two dislocation segments C_i and C_m which are part of the piecewise straight dislocation configuration of Figure 2, oriented as shown in Figure 4. A local, oblique x, y-coordinate system is generated from two unit vectors $\boldsymbol{\xi}_i$ and $\boldsymbol{\xi}_m$ aligned with the segments C_i and C_m, respectively. The positive senses of these two base vectors are determined by requiring the unit vector

$$\mathbf{e}_3 = \frac{\boldsymbol{\xi}_i \times \boldsymbol{\xi}_m}{|\boldsymbol{\xi}_i \times \boldsymbol{\xi}_m|}, \tag{3.1}$$

to be directed in the positive x_3-direction. The origin coincides with the point of intersection of the lines x and y, and θ is the angle between $\boldsymbol{\xi}_i$ and $\boldsymbol{\xi}_m$. In this coordinate system, the segment C_i has endpoint coordinates x_{i-1} and x_i, and the segment C_m has endpoint coordinates y_{m-1} and y_m. It is clear that the x and y axes lie on the glide plane of the threading dislocation, that is, the x_1, x_2-plane; see Figure 1.

It is convenient at this point to introduce the definitions

$$R(x,y) = \sqrt{x^2 + y^2 - 2xy\cos\theta}, \tag{3.2}$$

$$s(x,y) = R(x,y) + y - x\cos\theta, \tag{3.3}$$

$$t(x,y) = R(x,y) + x - y\cos\theta. \tag{3.4}$$

In terms of oblique coordinates, the dislocation energy E_{im} of two straight dislocation segments C_i and C_m, where $i \neq m$, is given by

$$E_{im} = \frac{\mu}{4\pi}\left\{(\mathbf{b}\cdot\boldsymbol{\xi}_i)(\mathbf{b}\cdot\boldsymbol{\xi}_m) + \frac{1}{1-\nu}[\mathbf{b}\cdot(\boldsymbol{\xi}_i \times \mathbf{e}_3)][\mathbf{b}\cdot(\boldsymbol{\xi}_m \times \mathbf{e}_3)]\right\} I(x_\alpha, y_\beta), \tag{3.5}$$

where

$$I(x,y) = x\log\frac{s(x,y)}{x} + y\log\frac{t(x,y)}{y} \tag{3.6}$$

and $I(x_\alpha, y_\beta)$ is a special summation of values of $I(x,y)$ at the endpoints of C_i and C_m defined as

$$I(x_\alpha, y_\beta) \equiv I(x_{i-1}, y_{m-1}) - I(x_{i-1}, y_m) - I(x_i, y_{m-1}) + I(x_i, y_m). \tag{3.7}$$

The dislocation energy associated with a dislocation segment, say C_i, interacting with itself ($i = m$) is given by

$$E_{ii} = \frac{\mu}{4\pi}\left[(\mathbf{b}\cdot\boldsymbol{\xi}_i)^2 + \frac{|\mathbf{b}\times\boldsymbol{\xi}_i|^2}{1-\nu}\right] L_i\left[\log\left(\frac{L_i}{\rho}\right) - 1\right], \tag{3.8}$$

where ρ is the core cutoff parameter, and L_i is the segment's length.

The expressions (3.5) and (3.8) for E_{im} and E_{ii} can be used to determine pointwise the dislocation's contribution to the energy $E(\bar{S})$ at each node a_i by means of the explicit summations in (2.3). Since each node a_i is shared by two dislocation segments C_i and C_{i+1}, the contributions to the dislocation energy at a_i can be assembled from three sources. First, consider the interaction of the segments C_i and C_{i+1} with segments C_m when $m < i$, that is

$$\sum_{m=0}^{i-1} E_{im} + \sum_{m=0}^{i-1} E_{(i+1)m}. \tag{3.9}$$

Similarly, the case $m > i$ and the case $m = i$, which corresponds to the interaction of the two segments sharing the node a_i must be considered. Finally, the contribution to the dislocation energy at a node associated with the self-interaction of the segments must be included. The applied-stress contribution to $E(\bar{S})$ is obtained by numerically integrating the third integral in (2.3) at each node.

To determine the nodal driving force G_i at a given node a_i, the derivative of $E(a_i)$ with respect to a_i must be formed according according to (2.4). This differentiation can be carried out on each individual contribution to $E(a_i)$, such as E_{im}. The driving force G_i can then be obtained from an assembly operation analogous to that which was described above for the dislocation energy. The individual contributions to G_i are derived in the Appendix. Results are included for nonadjacent segments (A.11) and (A.14), adjacent segments (A.17), segments interacting with semi-infinite segments (A.25), segments interacting with themselves (A.26), and the applied stress contribution (A.29).

4. Glide Kinetics and Time Integration

In the previous section expressions have been derived for the nodal forces G_i. These forces reflect the tendency of the dislocation to change its shape in order to decrease its elastic configurational energy. The nodal forces can be used in conjunction with the local kinetic equation (2.7) to obtain the nodal velocities v_i during glide along the embedded layer.

Consider once again the piecewise straight dislocation configuration of Figure 2. Restricting attention for the time being to the finite portion of this configuration, that is, excluding the two infinite segments, the appropriate expression for each unknown coefficient $v_o(i)$ at the i–th node in (2.7) are derived first. To this end, substituting for τ from (2.5) and for G_i from (2.7) in (2.9) results in

$$\int_B \left[v^{(m)}(\ell)\right]^2 \, d\ell = V_o h \sum_{i=0}^{N} \frac{v_i^2}{v_o(i)}, \tag{4.1}$$

where this expression holds strictly for the case of $E_o/kT = 1$. For the approximate configuration $\bar{B} = \sum_{i=1}^{N} C_i$, (4.1) can be rewritten as

$$\sum_{i=1}^{N} \int_0^{L_i} \left[v^{(m_i)}(\ell)\right]^2 \, d\ell = V_o h \sum_{i=0}^{N} \frac{v_i^2}{v_o(i)}, \tag{4.2}$$

where $v^{(m_i)}$ is the normal velocity of segment of C_i with outward normal $\mathbf{m}_i$, and the arclength ℓ is taken as positive when moving from node a_{i-1} towards node a_i. For a given straight segment C_i, the normal velocity $v^{(m_i)}(\ell)$ in terms of the nodal velocities and as a function of position along the segment is

$$v^{(m_i)}(\ell) = \frac{\cos\theta_i}{L_i}\left\{(L_i - \ell)v_{i-1} + \ell v_i\right\}, \tag{4.3}$$

where θ_i is the angle between the segment C_i and the horizontal datum. Therefore,

$$\int_0^{L_i} \left[v^{(m_i)}(\ell)\right]^2 \, d\ell = \frac{L_i}{3}\cos^2\theta_i (v_{i-1}^2 + v_{i-1}v_i + v_i^2). \tag{4.4}$$

Then, solving equation (4.2) for the nodal unknowns $v_o(i)$ yields

$$v_o(i) = \frac{3V_o h}{L_i \cos^2\theta_i + L_{i+1}\cos^2\theta_{i+1}} \qquad 1 \le i \le N-1. \tag{4.5}$$

Up to this point, the contributions of the two infinite segments C_0 and C_{N+1} have been excluded. The results can be extended to include these contributions by using (4.5) for the cases $i = 0$ and $i = N$, and taking the limit $L_0 \to \infty$ and $L_{N+1} \to \infty$ to obtain the trivial result

$$v_o(0) = v_o(N) = 0. \tag{4.6}$$

Equations (4.5) and (4.6), in conjunction with the results of section 3 for the nodal forces G_i, fully characterize the nodal velocities v_i as given by the kinetic equation (2.7). It remains to integrate these velocities in time in order to update the nodal coordinates a_i

At this point, it is convenient to express the driving force and velocities in dimensionless form. To this end, introduce the non-dimensional variables $\tilde{a}_i$, $\tilde{b}$, and $\tilde{\mu}$ through

$$a_i = \alpha \tilde{a}_i, \qquad b = \alpha \tilde{b}, \qquad \mu = \gamma \tilde{\mu}, \tag{4.7}$$

where α and γ have dimensions of length and stress, respectively. Then, the elastic interaction energy of the piecewise straight dislocation configuration which has the following independent variable dependence

$$E = E(a_o, \ldots, a_i, \ldots, a_N; b, \mu) \tag{4.8}$$

takes the following convenient reduction in dimensional dependence:

$$E(a_o, \ldots, a_i, \ldots, a_N; b, \mu) = \alpha^3 \gamma \widetilde{E}(\tilde{a}_o, \ldots, \tilde{a}_i, \ldots, \tilde{a}_N; \tilde{b}, \tilde{\mu}) \tag{4.9}$$

or,

$$E = \alpha^3 \gamma \widetilde{E}. \tag{4.10}$$

The definition of $\widetilde{E}$ should be clear in light of (4.9).

It is now a simple matter to express G_i and v_i in terms of their non-dimensional counterparts $\widetilde{G}_i$ and $\tilde{v}_i$. For the nodal forces it is found that

$$G_i = \alpha^2 \gamma \widetilde{G}_i, \tag{4.10}$$

where $\widetilde{G}_i = \partial \widetilde{E} / \partial \tilde{a}_i$. As for the nodal velocities, letting $\vartheta = (3V_o/\tilde{\mu}\tilde{b}) \exp(-Q_o/kT)$, which has dimensions of speed, the expression is

$$v_i = \vartheta \tilde{v}_i, \tag{4.11}$$

where

$$\tilde{v}_i = \frac{\widetilde{G}_i}{\widetilde{L}_i \cos^2 \theta_i + \widetilde{L}_{i+1} \cos^2 \theta_{i+1}}. \tag{4.12}$$

In this last expression, the lengths of the dislocation segments have been normalized by α.

From among the various ways in which the nodal velocities can be integrated in time, the simplest numerical time-integration scheme has been selected here, namely,

$$\tilde{a}_i^{n+1} = \tilde{a}_i^n + \widetilde{\Delta t}\, \tilde{v}_i^n \qquad 1 \le i \le N-1, \tag{4.13}$$

where the superscripts n and $n+1$ identify values at consecutive time steps. The non-dimensional time increment $\widetilde{\Delta t}$ in (4.13) is equal to $(\vartheta/\alpha)\Delta t$. As with all forward or explicit Euler time integration schemes, some sort of automatic time-step control is desirable in order to obtain accurate results from (4.13). A suitable local error associated with the integration at each node a_i is

$$e_i^n = \frac{|\widetilde{\Delta t}\,\nabla \tilde{v}_i^n|}{|\tilde{a}_i^n|}, \tag{4.14}$$

where $\nabla \tilde{v}_i^n = \tilde{v}_i^n - \tilde{v}_i^{n-1}$, that is, the first backward difference of $\tilde{v}_i^n$ (Press et al, 1986). Then the automatic time-step control can be achieved by controlling a global error associated with the entire configuration, say

$$e^n = \max_{1 \le i \le N-1} |e_i^n|. \tag{4.15}$$

5. Simulation of a Single Threading Dislocation

In this section, the motion of a single threading dislocation in an embedded strained epitaxial layer is simulated. The elastic mismatch strain in the layer is an isotropic extensional strain ϵ_o in the plane parallel to the interface. For definiteness, the layer is assumed to be the alloy Ge_xSi_{1-x}, where x is the fraction of lattice sites occupied by germanium atoms, and $1-x$ is the remaining fraction of sites occupied by silicon atoms. The numerical simulations are restricted to the $Ge_{.25}Si_{.75}$ alloy. The choice of material is motivated by experimental observations reported by Hull *et al.* (1988) for values of x between 0.25 and 0.3. The surrounding material is Si and the materials are oriented so that the normal to the interfaces is the [001] crystallographic direction. The threading dislocation glides on a $\{111\}$ plane which is inclined at an angle $\alpha = \sin^{-1}(1/\sqrt{3})$ with respect to the interface normal. In terms of x_1,x_2-coordinates, the components of the Burgers vector of the dislocation are $b_1 = \sqrt{3}b/2$ and $b_2 = -b/2$. The cutoff parameter ρ has been set at $b/8$. As the threading dislocation glides down the layer, it leaves behind a pair of straight 60° interface misfit dislocations, one on each interface.

Consider the behavior of a dislocation threading the layer. It is assumed that the layer thickness exceeds the critical thickness, so that the dislocation is unstable in the sense of elastic equilibrium theory, and the threading segment glides indefinitely far along the layer. Two basic questions that may be asked are: What is the magnitude of the driving force on the dislocation during the transient glide process, and what is the rate of misfit formation? This section addresses these two issues. In addition, the shape of the threading dislocation at various stages of the growth process is calculated.

Following a suggestion by Freund (1989), kinetic data for Ge_xSi_{1-x} films are estimated from available data on germanium and silicon by applying the rule of mixtures. Therefore parameters such as E_o, Q_o, and V_o which were introduced in section 2 are determined from

$$E_o = xE_g + (1-x)E_s, \quad Q_o = xQ_g + (1-x)Q_s, \quad V_o = xV_g + (1-x)V_s. \tag{5.1}$$

Based on data tabulated by Alexander (1986), $E_s = 0.064\,eV$, $Q_s = 1.69\,eV$, and $V_s = 1.36 \times 10^5\,m/s$ for silicon and $E_g = 0.195\,eV$, $Q_g = 0.307\,eV$, and $V_g = 1.145 \times 10^6\,m/s$ for germanium. Therefore, the kinetic data used for $Ge_{.25}Si_{.75}$ is $E_o = 9.68 \times 10^{-2}\,eV$, $Q_o = 1.34\,eV$, and $V_o = 3.88 \times 10^5\,m/s$. For this particular value of E_o, E_o/kT varies from 1.29 to 0.88 over a temperature range of 600-1000C, therefore the assumption that $E_o/kT \sim 1$ is a reasonable one over temperature ranges where experimental observations have been made.

Two case geometries have been considered, namely, $h = 1.1h_c$ and $h = 2h_c$. In both cases the mismatch strain $\epsilon_o = 0.02$. The simulations are carried out on the glide plane of the threading dislocation, the x_1,x_2–plane, where the uniform isotropic stress $\sigma_o = 2\mu\epsilon_o(1+\nu)/(1-\nu)$, acting in the plane of the layer, induces a resolved shear stress acting in the direction of the Burgers vector of the dislocation. This resolved traction is confined to the projected layer thickness on the glide plane, the thickness of which is $h_p = h/\cos\alpha$. For $h = 1.1h_c$, the normalized projected layer thickness h_p/b is 37.49. For $h = 2h_c$, the normalized projected layer thickness is 68.17. Outside the layer, a Peierls stress of magnitude $1 \times 10^{-3}\mu$ is applied to simulate the lattice resistance to the motion of the dislocation. The ratio of the Peierls stress to the resolved stress in the layer is 1:35 for $\nu = 0.3$.

The piecewise linear approximation of the threading dislocation is made up of three sections. The middle section – the layer section – consists of an odd number of evenly spaced nodes, the first node being on one of the interfaces and the last node being on the other interface. The nodal spacing is measured along the x_1-axis and is approximately equal to $9b$ in both cases. The other two sections – the "wing" sections – model the two sections of the dislocation line that lie outside the projected layer thickness. The ratio of the projected layer thickness to the length of the dislocation wings is approximately 1:10 in both cases. The outer node of a wing section lies on the x_1-axis and is attached to one of the semi-infinite elements discussed in the Appendix. The semi-infinite elements run along the x_1-axis and are not allowed to move during the kinetic simulation – in effect, the threading dislocation is pinned at two nodes which are relatively far from the interfaces.

At the start of the simulation the dislocation is straight and parallel to the x_1-axis. As the dislocation deforms and glides down the layer due to the elastic mismatch, the dislocation segments grow in size significantly, particularly the element on each wing closest to the layer. For this reason, an automatic remeshing scheme has been devised which subdivides these two dislocation segments based on their current lengths. The remeshing stops once the distance of the closest wing node to the interface reaches a critical minimum distance along the x_1-axis and the dislocation segment is nearly parallel to the interface. Due to the single degree-of-freedom formulation of the model, a dislocation segment that is parallel to the x_2-axis would be inadequate and would be unable to properly characterize the interaction of its two end-nodes.

Figure 5 shows the motion of the threading dislocation on a layer with thickness $h = 1.1h_c$ at an early non-steady stage of its growth history. The figure shows several configurations starting at time $\tilde{t} = 5 \times 10^3$ until time $\tilde{t} = 1.7 \times 10^5$ at regular time intervals $\widetilde{\Delta t} = 1.5 \times 10^4$. As was shown in section 4, the time scale used in the simulations is non-dimensional and real time can be obtained by multiplying the normalized time by $(\alpha/3V_o)\exp(Q_o/kT)$. For a temperature $T = 700K$ the dimensional factor is 1.52×10^{-6}s, for $T = 900$K it is 1.09×10^{-8}s, and for $T = 1200$K it is 1.45×10^{-10}s. The higher the temperature, the greater is the velocity of the dislocation. The asymmetry in the dislocation's shape, which has been observed by Hull and Bean (1990), for example, is due to the mixed nature of the Burgers vector. If the components of the Burgers vector were $b_1/b = 1$ and $b_2/b = 0$, then the dislocation would be symmetrical about the x_2-axis.

Figure 6 shows the long-term, steady-state motion of the dislocation. Here, the time interval $\widetilde{\Delta t}$ between configurations is 6×10^4. The first configuration shown in the figure is at $\tilde{t} = 5.5 \times 10^4$. The length of the misfit at $\tilde{t} = 4.75 \times 10^5$, the last frame in the figure, is approximately fifteen times the projected layer thickness. It is apparent from the figure that the velocity of the dislocation is nearly constant. Figure 7 shows non-dimensional values of the nodal driving force G_i for various nodes in the layer as a function of time. It is perhaps surprising that the forces acting on the nodes within the layer are different from each other, even though the nodes are all moving at essentially the same speed. Although all nodal forces were normalized in the same way in the kinetic equation (2.7), the coefficient $v_o(i)$ at any particular node depends on the configuration of the segments meeting at that node (cf. (4.5)). It is possible that some other scheme for normalizing G_i in (2.7) would result in the forces on nodes being equal when the nodal velocities are equal, but such a scheme has not yet been identified. Figure 8 shows the same information as a function of nodal position. The slight discontinuity in the figures (near $\tilde{t} = 5$ in Figure 7, say) is due to the remeshing procedure

described above. To obtain physical values from the non-dimensional force one must multiply the simulation data by $\alpha^2\gamma$, as shown in section 4. Assuming that $\gamma = 7.08 \times 10^3 \text{dynes}/\mu\text{m}^2$ (silicon) and a Burgers displacement of 4Å, this factor is 1.13×10^{-3}dynes. As these two figures show, initially the driving force is quite high, particularly on the center and inner nodes. With time, the force sharply drops and reaches a slowly decreasing plateau. In light of the discussion at the end of section 2, the driving force will reach an asymptotic steady-state value as $\tilde{t} \to \infty$. For practical purposes, though, the simulations reveal that this force becomes nearly constant after the misfit length is a few times the projected thickness length. The rate of misfit formation, which is given by the velocity of a node at the interface, is about $3.6V_o \exp(-Q_o/kT)$ when the driving force has reached a steady level.

Figure 9 shows the early stages of growth of a threading dislocation gliding down a layer with a thickness h that is 2 times the critical layer thickness h_c. Five configurations are shown, starting at $\tilde{t} = 1 \times 10^4$ and spaced at regular time intervals $\widetilde{\Delta t} = 1 \times 10^4$. The long term, steady-state motion of this dislocation is shown in Figure 10, where the first configuration is at $\tilde{t} = 7.5 \times 10^4$ and the time interval $\widetilde{\Delta t}$ between configurations is 2.5×10^4. The length of the misfit at $\tilde{t} = 2 \times 10^5$, the last frame in the figure, is approximately twenty times the projected layer thickness. The final time in Figure 10 is less than half of that in Figure 6. It is apparent that the dislocation shown in Figure 10 is gliding at a greater speed than that of the dislocation shown in Figure 6. This observation is consistent with equation (2.21) which reveals that the steady-state velocity v_{st} increases with increasing driving force G. Figure 11 shows non-dimensional values of the nodal driving force G_i for some of the layer nodes as a function of time, and Figure 12 shows the same information as function of position. The driving force on the center node is about five times larger than it is in Figure 8. Furthermore, the steady-state rate of misfit formation is about $22.3V_o \exp(-Q_o/kT)$, which is close to seven times faster than before.

6. Simulation of Interactions on Intersecting Glide Planes

Up to now, the numerical simulations have been restricted to the motion of a single threading dislocation through an embedded layer which is uniformly strained. Of interest are cases were a non-uniform strain distribution exists on the layer due to additional traction on the glide plane. The non-uniform strain distribution changes the driving force acting on the threading dislocation. In this section, one such case is considered, namely, the blocking of a threading dislocation by an interface misfit dislocation lying on an intersecting glide plane. The specific configuration to be considered is shown in Figure 13. For the remainder of this section, the coordinate axis labels adopted previously will be dropped in favor of those shown in the figure. The two glide planes shown are intersecting {111}-planes. These planes are identified on the pyramids of close-packed {111}-planes in a cubic material in Figure 14. As in section 5, the embedded layer and the surrounding material are assumed to be $Ge_{0.25}Si_{0.75}$ and Si, respectively, and the normal to the interfaces is the [001] crystallographic direction. With respect to the base vectors of the x_1, x_2, x_3–coordinate system, the normal to the x_2, x_3'–plane is the vector $\{\sqrt{2/3}, 0, \sqrt{1/3}\}$ and the normal to the x_1, x_3''–plane is the vector $\{0, \sqrt{2/3}, \sqrt{1/3}\}$.

As shown in Figure 13, the threading dislocation glides on the x_2, x_3'–plane in the positive x_2-direction, and it is assumed that its Burgers vector lies in this plane. A misfit dislocation, modelled by an infinite straight dislocation, lies along the x_1-axis; its Burgers vector is assumed to lie in the x_1, x_3''–plane. Image effects associated with the interfaces will be ignored. As discussed by Freund (1989), there are several possible combinations of Burgers vectors, but only cases were both dislocations relieve elastic strain in the layer are of interest. The possible directions of Burgers vectors for the two dislocations are represented by the edges of the two shaded planes in Figure 14. These correspond to eight combinations of Burgers vectors with components in the x_3-direction. These combinations are reproduced below in Table 1 as they were listed by Freund (1989).

Table 1

(i)	$\left\{-\frac{1}{2},\frac{1}{2},-\sqrt{\frac{1}{2}}\right\}$	$\left\{-\frac{1}{2},-\frac{1}{2},\sqrt{\frac{1}{2}}\right\}$
(ii)	$\left\{\frac{1}{2},\frac{1}{2},-\sqrt{\frac{1}{2}}\right\}$	$\left\{-\frac{1}{2},-\frac{1}{2},\sqrt{\frac{1}{2}}\right\}$
(iii)	$\left\{-\frac{1}{2},\frac{1}{2},\sqrt{\frac{1}{2}}\right\}$	$\left\{-\frac{1}{2},-\frac{1}{2},\sqrt{\frac{1}{2}}\right\}$
(iv)	$\left\{\frac{1}{2},\frac{1}{2},\sqrt{\frac{1}{2}}\right\}$	$\left\{-\frac{1}{2},-\frac{1}{2},\sqrt{\frac{1}{2}}\right\}$
(v)	$\left\{-\frac{1}{2},\frac{1}{2},-\sqrt{\frac{1}{2}}\right\}$	$\left\{-\frac{1}{2},\frac{1}{2},\sqrt{\frac{1}{2}}\right\}$
(vi)	$\left\{\frac{1}{2},\frac{1}{2},-\sqrt{\frac{1}{2}}\right\}$	$\left\{-\frac{1}{2},\frac{1}{2},\sqrt{\frac{1}{2}}\right\}$
(vii)	$\left\{-\frac{1}{2},\frac{1}{2},\sqrt{\frac{1}{2}}\right\}$	$\left\{-\frac{1}{2},\frac{1}{2},\sqrt{\frac{1}{2}}\right\}$
(viii)	$\left\{\frac{1}{2},\frac{1}{2},\sqrt{\frac{1}{2}}\right\}$	$\left\{-\frac{1}{2},\frac{1}{2},\sqrt{\frac{1}{2}}\right\}$

The magnitudes of the two Burgers vectors are assumed to be the same. Moreover, the components of the vectors are referred to unit base vectors of the x_1, x_2, x_3–coordinate system.

The stress field arising from the misfit dislocation along the x_1-axis sets up an additional contribution to the applied stress field σ^A in (2.1). Denote this additional stress field by σ^I for the present discussion. This field is given by the stress field of a straight dislocation in an unbounded body. Hence, the stress field corresponding to the edge component of the misfit dislocation depends only on position in the x_2, x_3–plane, and it can be computed from the Airy stress function

$$\chi(x_2, x_3) = \frac{\mu(b_3 x_2 - b_2(x_3 + h/2))}{4\pi(1-\nu)} \log\sqrt{x_2^2 + (x_3 + h/2)^2} \tag{6.1}$$

according to

$$\sigma_{22}^I = \frac{\partial^2 \chi}{\partial x_3^2}, \quad \sigma_{33}^I = \frac{\partial^2 \chi}{\partial x_2^2}, \quad \sigma_{23}^I = -\frac{\partial^2 \chi}{\partial x_2 \partial x_3}, \quad \sigma_{11}^I = \nu(\sigma_{22}^I + \sigma_{33}^I). \tag{6.2}$$

The stress field associated with the screw component of the Burgers vector of the straight dislocation is

$$\sigma_{12}^I = -\frac{\mu b_1}{4\pi} \frac{(x_3 + h/2)}{x_2^2 + (x_3 + h/2)^2}, \quad \sigma_{13}^I = \frac{\mu b_1}{4\pi} \frac{x_2}{x_2^2 + (x_3 + h/2)^2}. \tag{6.3}$$

The above stress distribution gives rise to a resolved shear stress $\tau = [\mathrm{b} \cdot (\sigma^I \cdot \mathrm{n})]/b$ in the direction of the Burgers vector on the x_2, x_3'–plane. This stress can increase or decrease the magnitude of the nodal driving force G_i on the dislocation. The interaction nodal driving force G_i^I is estimated by the method of the Appendix A.5. Instead of the linear quadrature rule used in that section to integrate the contribution of the misfit strain, a suitable quadrature rule, that takes into account the fact that the stress field σ^I decreases as one over the radial distance to the misfit dislocation, is used.

The two layer geometries studied in section 5, namely, $h = 1.1h_c$ and $h = 2h_c$, have been reconsidered, and once again the mismatch strain ϵ_o in the embedded layer is 0.02. The numerical simulations are carried out for the Burgers vector combination (i) as defined in Table 1. For this combination, the non-uniform strain distribution encountered by the advancing glide dislocation is such that its driving force is reduced as it approaches the misfit dislocation from the negative x_2-direction; see Freund (1989, 1990) for more details.

At the beginning of the simulation, the threading dislocation starts parallel to the x_3'-axis at $x_2 = -l$, where l is some suitable distance from the origin. The straight misfit is always positioned at $x_2 = 0$ and $x_3' = h/2\cos\alpha$. For the first case, $h = 1.1h_c$, simulations where done for values of $l = 150b$, $300b$, and $600b$. Figure 15 shows a sequence of configurations leading to the blocking of the threading dislocation by a misfit. The first configuration shown is at time $\tilde{t} = 2.5 \times 10^4$ and the last one, at $\tilde{t} = 6.5 \times 10^4$. The time interval between configurations is $\widetilde{\Delta t} = 5 \times 10^3$. The threading dislocation was started at $x_2 = -150b$. Figure 16 shows non-dimensional values of the nodal driving force G_i for the center layer node and the interfacial node as a function of nodal position along the x_2-axis. The dotted curves corresponding to values of G_i in the absence of a misfit are shown for comparison. The figure shows that the driving force on the threading dislocation remains unaffected until the dislocation is within a radius of $25b$ from the misfit. At this point, the near field of the straight dislocation becomes dominant and decreases the driving force quite severely. This slows down the gliding dislocation which ultimately arrests. The numerical simulation presented here is unsuitable for predicting configurational issues after the interfacial segment of the threading dislocation intersects the misfit. At this point, a dislocation reaction would take place, resulting in the formation of a jog or a kink. A realistic simulation would have to take into account the newly created dislocation segment.

In order to illustrate the slow-down of the gliding dislocation due to the presence of a misfit, Figure 17 shows a superposition of sequences of configurations. The solid curves correspond to a gliding dislocation being blocked, the dotted curves correspond to a dislocation gliding in the absence of a misfit. The initial configurations shown are at time $\tilde{t} = 1 \times 10^5$ and the last ones, at $\tilde{t} = 1.5 \times 10^5$. The time interval between configurations is $\widetilde{\Delta t} = 1 \times 10^4$. The threading dislocation was started at $x_2 = -300b$. It is apparent from the figure that the slow-down is significant. Figure 18 shows non-dimensional values of the nodal driving force G_i for the center layer node and the interfacial node as a function of nodal position along the x_2-axis. Finally, Figure 19 shows non-dimensional values of the nodal driving force G_i for the center layer node and the interfacial node

as a function of nodal position along the x_2-axis, for the case where the threading dislocation is started at $x_2 = -600b$. Here, the magnitude of the driving force on the gliding dislocation is rather low as the dislocation approaches the misfit at $x_2 = 0$, so only a small change in G is required for the dislocation to arrest.

Results for the second layer geometry, $h = 2h_c$, are very similar to those illustrated above for $h = 1.1h_c$. Figure 20 shows a sequence of configurations leading to the blocking of the threading dislocation by a misfit. The threading dislocation was started at $x_2 = -300b$. As discussed in section 5, for this configuration the driving force is much higher and consequently it is more difficult to arrest nodes in the middle of the layer. Figure 21 shows non-dimensional values of the nodal driving force G_i for the mid-layer node, an intermediate node, and the interfacial node as a function of nodal position along the x_2-axis. In contrast with the case of $h = 1.1h_c$, the middle node is barely affected by the stress field of the straight misfit. Consequently, the slow-down is less dramatic.

Acknowledgments

This work has been supported by an IBM Research Award in Materials Science, by the Office of Naval Research through contract N00014-87-K-0481, and by the National Science Foundation through grant DMR87-14665. This support is gratefully acknowledged.

References

- H. Alexander, "Dislocations in covalent crystals," in *Dislocations in Solids*, vol. 7, edited by F. R. N. Nabarro, Elsevier Science Publishers, pp.115–234 (1986).
- J. C. Bean, "Strained-layer epitaxy of germanium-silicon alloys," *Science* 230 (1985) 127-131.
- B. W. Dodson and P. A. Taylor, "Atomistic Monte Carlo calculation of critical layer thickness for coherently strained silicon-like structures," *Appl. Phys. Lett.*, vol. 49, pp. 642–644 (1986).
- B. W. Dodson and J. Y. Tsao, "Relaxation of strained layer semiconductor structures via plastic flow", *Appl. Phys. Lett.* **51**, 1325 (1987).
- J. Dundurs, "Elastic interaction of dislocations with inhomogenieties," in *Mathematical Theory of Dislocations*, ASME, pp. 70–115 (1969).
- D. J. Eaglesham, E. P. Kvam, D. M. Maher, C. J. Humphreys and J. C. Bean, "Dislocation nucleation near the critical thickness in GeSi/Si strained layers", *Phil. Mag.* **A59**, 1059 (1989).
- E. A. Fitzgerald, G. P. Watson, R. E. Proano, D. G. Ast, P. D. Kirchner, G. D. Petit and J. M. Woodall, "Nucleation mechanisms and the elimination of misfit dislocations at mismatched interfaces by reduction in growth area", *J. Appl. Phys.* **65**, 2220 (1989).
- L. B. Freund, "The Stability of a dislocation threading a strained layer on a substrate," *J. Appl. Mech.*, vol. 54, pp. 553–557 (1987).
- L. B. Freund, A. Bower, and J.-C. Ramirez, "Mechanics of elastic dislocations in strained layer structures," in *Thin Films: Stresses and Mechanical Properties*, MRS Symposium Proceedings vol. 130, edited by J. C. Bravman *et al.*, Materials Research Society, pp. 139–152 (1989).
- L. B. Freund, "The driving force for glide of a threading dislocation in a strained epitaxial layer on a substrate," *J. Mech. Phys. Solids* (1990, to appear).
- L. B. Freund, "A criterion for arrest of a threading dislocation in a strained epitaxial layer due to an interface misfit dislocation in its path", *J. Appl. Physics* (1990, to appear).
- J. P. Hirth and J. Lothe, *Theory of Dislocations*, Second Edition, McGraw-Hill (1982).
- R. Hull, J. C. Bean, D. J. Werder, and R. E. Leibenguth, "In situ observations of misfit dislocation propagation in Ge_xSi_{1-x}/Si(100) heterostructures," *Appl. Phys. Lett.*, vol. 52, pp. 1605–1607 (1988).

- R. Hull, J. C. Bean, D. J. Eaglesham, J. M. Bonar and C. Beuscher, "Strain relaxation phenomena in Ge_xSi_{1-x}/Si strained layer structures", *Thin Solid Films* **183**, 117 (1989).
- R. Hull and J. C. Bean, in *Layered Structures-Heteroepitaxy, Superlattices, Strain and Metastability*, edited by L. J. Schowalter, B. W. Dodson, F. H. Pollak and J. E. Cunningham, (MRS Proc. **160**, Pittsburgh, 1990), to appear.
- J. W. Matthews, S. Mader, and T. B. Light, "Accommodation of misfit across the interface between crystals of semiconducting elements or compounds," *J. Appl. Phys.*, vol. 41, pp. 3800–3804 (1970).
- W. H. Press, B. P. Flannery, S. A. Teukolsky and W. T. Vettering, *Numerical Recipes*, Cambridge University Press (1986).
- J. Y. Tsao and B. W. Dodson, "Excess stress and the stability of strained heterostructures", *Appl. Phys. Lett.* **53**, 848 (1988).
- C. G. Tuppen, C. J. Gibbings and M. Hockly in *Thin Films: Stresses and Mechanical Properties*, edited by J. C. Bravman, W. D. Nix, D. M. Barnett and D. A. Smith (MRS Proc. **130**, Pittsburgh, PA 1989) 185-190.

Appendix: Expressions for Nodal Driving Forces

A.1 Nonadjacent Interacting Segments

Consider a segment C_{i+1} with end nodes a_i and a_{i+1} interacting with a second disjoint segment, say C_{m+1}, with end nodes a_m and a_{m+1}. Figure 22 shows the geometry for this case. The nodal coordinates a_i, a_{i+1}, a_m, and a_{m+1} are measured from a common horizontal datum as was described in section 2. The horizontal distance between the ends of the segment C_{i+1} is d_{i+1}; for the segment C_{m+1}, this distance is d_{m+1}. From the geometry it is found that the nodal coordinates in the oblique x, y, z-system are

$$x_i = -X\sqrt{1 + \frac{(a_{i+1} - a_i)^2}{d_{i+1}^2}}, \tag{A.1}$$

$$x_{i+1} = x_i + L_{i+1}, \tag{A.2}$$

$$y_m = (D - X)\sqrt{1 + \frac{(a_{m+1} - a_m)^2}{d_{m+1}^2}}, \tag{A.3}$$

$$y_{m+1} = y_m + L_{m+1}, \tag{A.4}$$

where

$$X = \frac{D(a_{m+1} - a_m)d_{i+1} - (a_m - a_i)d_{i+1}d_{m+1}}{(a_{m+1} - a_m)d_{i+1} - (a_{i+1} - a_i)d_{m+1}}, \tag{A.5}$$

$$L_{i+1} = \sqrt{(a_{i+1} - a_i)^2 + d_{i+1}^2}, \tag{A.6}$$

$$L_{m+1} = \sqrt{(a_{m+1} - a_m)^2 + d_{m+1}^2}, \tag{A.7}$$

and D is the horizontal distance between nodes a_i and a_m.

In light of (3.5), the interaction energy between the two segments is

$$E_{i+1(m+1)} = \frac{\mu}{4\pi}\frac{1}{L_{i+1}L_{m+1}}\left[f_{i+1}f_{m+1} + \frac{g_{i+1}g_{m+1}}{1 - \nu}\right]I(x_\alpha, y_\beta), \tag{A.8}$$

where

$$f_r = d_r b_1 + (a_r - a_{r-1})b_2, \tag{A.9}$$

$$g_r = (a_r - a_{r-1})b_1 - d_r b_2. \tag{A.10}$$

It follows that the rate of change of the dislocation energy with respect to nodal position is

$$\frac{\partial}{\partial a_i}E_{i+1(m+1)} = \frac{\mu}{4\pi}\frac{1}{L_{i+1}L_{m+1}}\left\{-\left[b_2 f_{m+1} + \frac{b_1 g_{m+1}}{1 - \nu}\right]I(x_\alpha, y_\beta)\left[f_{i+1}f_{m+1} + \frac{g_{i+1}g_{m+1}}{1 - \nu}\right]\times \right.$$
$$\left.\left[\frac{\partial}{\partial a_i}I(x_\alpha, y_\beta) - \frac{(a_i - a_{i+1})}{L_{i+1}^2}I(x_\alpha, y_\beta)\right]\right\}. \tag{A.11}$$

In the above expression, $\partial I(x_\alpha, y_\beta)/\partial a_i$ can be written as $\sum_{\alpha=1}^{2}(H_\alpha + J_\alpha)$, where the functions H_α and J_α are defined as

$$H_\alpha = \frac{\partial x_\alpha}{\partial a_i}\log\frac{s_{\alpha\alpha}}{s_{\alpha(3-\alpha)}} + \frac{\partial y_\alpha}{\partial a_i}\log\frac{t_{\alpha\alpha}}{t_{(3-\alpha)\alpha}}, \tag{A.12}$$

$$J_\alpha = \frac{x_\alpha}{s_{\alpha\alpha}s_{\alpha(3-\alpha)}}\left\{\frac{\partial s_{\alpha\alpha}}{\partial a_i}s_{\alpha(3-\alpha)} - s_{\alpha\alpha}\frac{\partial s_{\alpha(3-\alpha)}}{\partial a_i}\right\} + \frac{y_\alpha}{t_{\alpha\alpha}t_{(3-\alpha)\alpha}}\left\{\frac{\partial t_{\alpha\alpha}}{\partial a_i}t_{(3-\alpha)\alpha} - t_{\alpha\alpha}\frac{\partial t_{(3-\alpha)\alpha}}{\partial a_i}\right\}. \tag{A.13}$$

In these last two expressions, $s_{\alpha(3-\alpha)}$ denotes the function $s(x,y)$, as defined in (3.3), evaluated at $x = x_\alpha$ and $y = y_{3-\alpha}$. It has no connection with the notation introduced in (3.7) for $I(x,y)$. Derivatives such as $\partial s_{\alpha\alpha}/\partial a_i$ are readily obtained from expressions displayed in this section and the details are omitted.

Another instance of interaction of nonadjacent segments consists of a segment with end nodes a_{i-1} and a_i interacting with a second segment with end nodes a_m and a_{m+1}. Figure 23 shows the geometry for this case. The previous analysis holds for this case as well if a_i is replaced by a_{i-1}, a_{i+1} by a_i, and so on, and corresponding algebraic signs are changed. It follows that the rate of change of interaction energy for this case is

$$\frac{\partial}{\partial a_i}E_{i(m+1)} = \frac{\mu}{4\pi}\frac{1}{L_iL_{m+1}}\left\{\left[b_2f_{m+1} + \frac{b_1g_{m+1}}{1-\nu}\right]I(x_\alpha, y_\beta) + \left[f_if_{m+1} + \frac{g_ig_{m+1}}{1-\nu}\right]\left[\frac{\partial}{\partial a_i}I(x_\alpha, y_\beta) - \frac{(a_i - a_{i-1})}{L_i^2}I(x_\alpha, y_\beta)\right]\right\}. \tag{A.14}$$

A.2 Adjacent Interacting Segments

Next, the interaction of two adjacent dislocation segments which share the node a_i is considered. Figure 24 illustrates this situation where the nodal coordinates have been chosen as $x_i = 0$, $x_{i+1} = L_{i+1}$, $y_{i-1} = -L_i$, and $y_i = 0$. The lengths L_{i+1} and L_i of the x_ix_{i+1} and $y_{i-1}y_i$ segments are given by

$$L_{i+1} = \sqrt{(a_{i+1} - a_i)^2 + d_{i+1}^2}, \tag{A.15}$$

$$L_i = \sqrt{(a_i - a_{i-1})^2 + d_i^2}, \tag{A.16}$$

An analysis analogous to that presented in section A.1 reveals that the rate of change of dislocation energy for adjacent segments is

$$\begin{aligned}\frac{\partial}{\partial a_i}E_{i(i+1)} = \frac{\mu}{4\pi}\frac{1}{L_iL_{i+1}}\Bigg\{&\left[b_2(f_{i+1} - f_i) + \frac{b_1(g_{i+1} - g_i)}{1-\nu}\right]I(x_\alpha, y_\beta) \\ &+ \left[f_{i+1}f_i + \frac{g_{i+1}g_i}{1-\nu}\right]\left[\frac{\partial}{\partial a_i}I(x_\alpha, y_\beta) - \left(\frac{1}{L_i}\frac{\partial L_i}{\partial a_i} + \frac{1}{L_{i+1}}\frac{\partial L_{i+1}}{\partial a_i}\right)\times\right. \\ &\left.I(x_\alpha, y_\beta)\right]\Bigg\}.\end{aligned} \tag{A.17}$$

A.3 Segment Interacting with Infinite Segments

The case of a segment interacting with two semi-infinite segments requires special attention. As was mentioned in section 2, the semi-infinite segments are necessary to model arbitrarily long dislocations, but are not needed to model finite dislocation loops. Figure 25 shows a segment C_{i+1} with end nodes a_i and a_{i+1} and two infinite segments $y_1'y_2'$ and $y_1''y_2''$. In the figure, the length of an infinite segment is shown to be m, but the limiting case $m \to \infty$ is of primary interest. A difficulty associated with determining the energy of interaction of the dislocation configuration shown in Figure 25 is the fact that this energy is unbounded as $m \to \infty$. A solution to this problem is to consider the energy increase in going from a reference configuration consisting of segments $y_1'y_2'$ and $y_1''y_2''$, and the dummy segment y_iy_{i+1}, to one consisting of segments $y_1'y_2'$, x_ix_{i+1}, and $y_1''y_2''$. This is the same procedure that was followed in the example at the end of section 2 to obtain the energy associated with the formation of a kink. The energy change is

$$\Delta E_{inf} = E(y_1'y_2' : x_ix_{i+1}) + E(x_ix_{i+1} : y_1''y_2'') - E(y_1'y_2' : y_iy_{i+1}) - E(y_1''y_2'' : y_iy_{i+1}). \tag{A.18}$$

This energy change is finite in the limit as $m \to \infty$ because the singularities associated with the two semi-infinite dislocation segments cancel each other out. Moreover, the final expression for G_i

is unaffected by the choice of ΔE_{inf} over that of E_{inf} because the reference configuration does not depend on the nodal coordinate a_i.

The first term $E(y_1'y_2' : x_ix_{i+1}) + E(x_ix_{i+1} : y_1''y_2'')$ is given by

$$E(y_1'y_2' : x_ix_{i+1}) + E(x_ix_{i+1} : y_1''y_2'') = \frac{\mu b^2}{4\pi} \cos\theta \; I(x_\alpha, y_\beta), \tag{A.19}$$

where $I(x_\alpha, y_\beta)$ can be decomposed additively into a non-singular term $I_{0,im}$ and a singular term $I_{m,im}$. The implication is that the former term remains bounded in the limit as $m \to \infty$, whereas the latter term does not. These two contributions can be written explicitly as

$$I_o(x_\alpha, y_\beta) = x_i \log \frac{s_{i1}''}{s_{i2}'} + x_{i+1} \log \frac{s_{(i+1)2}'}{s_{(i+1)1}''} + y_1'' \log \frac{t_{i1}''}{t_{(i+1)1}''} + y_2'' \log \frac{t_{(i+1)2}'}{t_{i2}'}, \tag{A.20}$$

and

$$I_m(x_\alpha, y_\beta) = x_i \log \frac{s_{i1}'}{s_{i2}''} + x_{i+1} \log \frac{s_{(i+1)2}''}{s_{(i+1)1}'} + y_1' \log \frac{t_{i1}'}{t_{(i+1)1}'} + y_2'' \log \frac{t_{(i+1)2}''}{t_{i2}''}. \tag{A.21}$$

In equations (A.20) and (A.21) some abbreviated notation has been adopted. For instance, $s_{i1}' = s(x_i, y_1')$ where $s(x, y)$ has been defined in (A.3).

The remaining terms in (A.18) are

$$E(y_1'y_2' : y_iy_{i+1}) + E(y_1''y_2'' : y_iy_{i+1}) = \frac{\mu b^2}{4\pi} I(x_\alpha, y_\beta), \tag{A.22}$$

where it can be shown that

$$I(x_\alpha, y_\beta) = d_{i+1} \log \frac{(D'' - d_{i+1} + m)(D' + d_{i+1} + m)}{(D' + d_{i+1})(D'' - d_{i+1})} - D'' \log \frac{D''}{D'' - d_{i+1}} - D' \log \frac{D' + d_{i+1}}{D'} + 2d_{i+1}. \tag{A.23}$$

The definitions of D'', D', and d_{i+1} should be clear from Figure 25.

Combining all the terms in (A.18) and taking the limit $m \to \infty$ yields

$$\Delta E_{inf} = \frac{\mu b^2}{4\pi} \cos\theta \left\{ I_o(x_\alpha, y_\beta) + 2x_i \log x_i - 2x_{i+1} \log x_{i+1} - \frac{2d_{i+1}}{\cos\theta} \log \frac{\sin\theta}{2} \right\} + \frac{\mu b^2}{4\pi} \left\{ (d_{i+1} - D'') \log(D'' - d_{i+1}) + D' \log D' + (d_{i+1} - D') \log D' + d_{i+1} \right\}. \tag{A.24}$$

The above result is a generalization of equation (2.11). Finally, the rate of change of the dislocation energy with respect to nodal position is found to be

$$\frac{\partial E_{inf}}{\partial a_i} = -\frac{\mu b^2}{4\pi}\frac{(a_i - a_{i+1})}{L_{i+1}^2}\frac{d_{i+1}}{L_{i+1}}\left\{I_o(x_\alpha, y_\beta) + 2x_i \log x_i - 2x_{i+1}\log x_{i+1}\right\} +$$
$$\frac{\mu b^2}{4\pi}\frac{d_{i+1}}{L_{i+1}}\left\{\frac{\partial}{\partial a_i}I_o(x_\alpha, y_\beta) + 2\log x_i \frac{\partial x_i}{\partial a_i} - 2\log x_{i+1}\frac{\partial x_{i+1}}{\partial a_i}\right.$$
$$\left. - 2\frac{\partial L_{i+1}}{\partial a_i} - 2\frac{d_{i+1}}{\sin\theta}\frac{\partial \theta}{\partial a_i}\right\}. \qquad (A.25)$$

In addition to the interaction of a dislocation segment with two infinite segments, there are two other special interactions of nonadjacent segments which must be considered in order to successfully implement the numerical scheme. Both cases come about when the coordinate system described in the introduction of this section breaks down. The first involves colinear segments, either adjacent or nonadjacent. The second case involves the interaction of parallel nonadjacent segments. Suitable expressions can be derived as limiting cases of the equations derived in sections A.1 and A.2. The case of parallel segments is discussed by Hirth and Lothe (1982).

A.4 Self-Interacting Segment

Finally, to conclude the derivation of the contribution to the nodal forces associated with the dislocation self-stress σ^D, the dislocation energy associated with self-interacting segments is considered. Once again, attention is focussed on the geometry of Figure 2-1 which shows that the node a_i contributes to the dislocation energy E_{ii} of two dislocation segments. Making use of equation (3.8) and some of the results of section A.2, it is found that the rate of change of energy with respect to nodal position is

$$\frac{\partial E_{ii}}{\partial a_i} = -\frac{\mu}{2\pi L_{i+1}}\left[b_2 f_{i+1} + \frac{b_1 g_{i+1}}{1-\nu}\right]\log\left(\frac{L_{i+1}}{e\rho}\right) + \frac{\mu}{2\pi L_i}\left[b_2 f_i + \frac{b_1 g_i}{1-\nu}\right]\log\left(\frac{L_i}{e\rho}\right)$$
$$- \frac{\mu}{4\pi}\left[f_{i+1}^2 + \frac{g_{i+1}^2}{1-\nu}\right]\frac{(a_{i+1} - a_i)}{L_{i+1}^3}\log\left(\frac{L_{i+1}}{\rho}\right)$$
$$+ \frac{\mu}{4\pi}\left[f_i^2 + \frac{g_i^2}{1-\nu}\right]\frac{(a_i - a_{i-1})}{L_i^3}\log\left(\frac{L_i}{\rho}\right) \qquad (A.26).$$

A.5 Applied Stress Contribution

The elastic interaction energy associated with the work done during glide by the applied stresses acting on the glide plane was first introduced in equation (2.1). This energy can be written as

$$E_A(S) = \int_S b\tau \, dS, \tag{A.27}$$

where the subscript A is used to indicate that $E_A(S)$ is the contribution to the interaction energy $E(S)$ due to the resolved shear stress in the direction of the Burgers vector $\tau = [\mathbf{b} \cdot (\boldsymbol{\sigma}^A \cdot \mathbf{n})]/b$ on the glide plane S.

We wish to determine the nodal force G_i^A which is given by the rate of change of $E_A(\bar{S})$ with respect to the position of the approximate dislocation configuration. Unlike the stress field $\boldsymbol{\sigma}^D$, the applied stress field $\boldsymbol{\sigma}^A$ is arbitrary and is one of the input variables of the model. In most cases, it is necessary to evaluate the integral in (A.27) numerically. The simplest quadrature rule is obtained by assuming that, for each dislocation segment C_i, τ is a function of position along the segment and depends linearly on the values at the nodes. In other words,

$$\tau(\ell) = \tau_{i-1} + \frac{\ell}{L_i}(\tau_i - \tau_{i-1}) \qquad 0 \le \ell \le L_i, \tag{A.28}$$

where τ_{i-1} and τ_i are the values of τ at the nodes a_{i-1} and a_i of the segment C_i of length L_i, and the sense of the arclength ℓ is from node a_{i-1} to node a_i.

In light of (A.28), it can be shown that the rate of change of $E_A(\bar{S})$ with respect to to a change in a_i, while holding all other nodes fixed, is given by

$$G_i^A = b\left\{\frac{1}{6}d_i\tau_{i-1} + \frac{1}{3}(d_i + d_{i+1})\tau_i + \frac{1}{6}d_{i+1}\tau_{i+1}\right\}, \tag{A.29}$$

where d_i and d_{i+1} are the horizontal distances between the nodes a_{i-1} and a_i and between a_i and a_{i+1}, respectively.

FIGURE CAPTIONS

Fig. 1 A threading dislocation gliding down the x_1, x_2-plane between an embedded strained layer of thickness h and two half-spaces. The threading dislocation extends from the half-spaces through the layer, and it then continues along each of the interfaces as a mismatch dislocation.

Fig. 2 A discrete approximation of the actual configuration of Figure 1 consisting of $N + 2$ linear dislocation segments. The numerical simulations are carried out in the x_1, x_2-plane, the glide plane of the threading dislocation.

Fig. 3 The simplest of discrete approximations to the configuration of Figure 1. The glide plane of the dislocation, the x_1, x_2-plane, is inclined at an angle α from the normal to the bi-material interface.

Fig. 4 Two dislocation segments C_i and C_m which are part of the piecewise configuration of Figure 2 in a local, oblique x, y-coordinate system.

Fig. 5 The motion in the x_1, x_2-plane of the threading dislocation at an early non-steady stage of its growth history. The thickness of the embedded layer is 1.1 times the critical thickness.

Fig. 6 The long-term, steady-state motion of the threading dislocation in the x_1, x_2-plane. The thickness of the embedded layer is 1.1 times the critical thickness.

Fig. 7 Non-dimensional values of the nodal driving force G_i for various nodes in the layer as a function of time. The time normalization factor t_0 is equal to $(b/3V_o)\exp(Q_o/kT)$. The labels on the curves correspond to x_1 coordinates of the nodes in terms of the projected layer thickness h_p. The embedded layer's thickness is 1.1 times the critical thickness.

Fig. 8 Non-dimensional values of the nodal driving force G_i for various nodes in the layer as a function of nodal position. The labels on the curves correspond to x_1 coordinates of the nodes in terms of the projected layer thickness h_p. The thickness of the embedded layer is 1.1 times the critical thickness.

Fig. 9 The motion in the x_1, x_2-plane of the threading dislocation at an early non-steady stage of its growth history. The thickness of the embedded layer is two times the critical thickness.

Fig. 10 The long-term, steady-state motion of the threading dislocation in the x_1, x_2-plane. The thickness of the embedded layer is two times the critical thickness.

Fig. 11 Non-dimensional values of the nodal driving force G_i for various nodes in the layer as a function of time. The time normalization factor t_0 is equal to $(b/3V_o)\exp(Q_o/kT)$. The labels on the curves correspond to x_1 coordinates of the nodes in terms of the projected layer thickness h_p. The thickness of the embedded layer is two times the critical thickness.

Fig. 12 Non-dimensional values of the nodal driving force G_i for various nodes in the layer as a function of nodal position. The labels on the curves correspond to x_1 coordinates of the nodes in terms of the projected layer thickness h_p. The thickness of the embedded layer is two times the critical thickness.

Fig. 13 An embedded strained layer and two intersecting glide planes. The threading dislocation glides on the x_2, x_3'-plane in the positive x_2-direction. A misfit dislocation lies along the x_1-axis.

Fig. 14 Pyramids of the close-packed {111} planes in a cubic crystal showing the various glide planes. The crystallographic direction normal to the interface is [001]. The Burgers vector of the threading dislocation on the shaded plane coincides with either of the edges *aq* or *bq*, while the Burgers vector of the straight dislocation lying along *ad* coincides with either *ap*, *dp*, *aq* or *dq*.

Fig. 15 The motion in the x_2, x_3'-plane of a threading dislocation that was started at $x_2 = -150b$. A misfit dislocation is positioned at $x_2 = 0$ and $x_3' = h/2\cos\alpha$. The thickness of the embedded layer is 1.1 times the critical thickness.

Fig. 16 Non-dimensional values of the nodal driving force G_i for the center node ($x_3' = 0$) and the interfacial node ($x_3'/b = h_p/2$) as a function of nodal position. The dotted curves correspond to the driving force in the absence of the blocking misfit. The threading dislocation was started at $x_2 = -150b$.

Fig. 17 A close-up of the motion in the x_2, x_3'-plane of a threading dislocation that was started at $x_2 = -300b$ in the vicinity of a blocking misfit. The misfit dislocation is positioned at $x_2 = 0$ and $x_3' = h/2\cos\alpha$. The dotted curves correspond to the motion of the same threading dislocation in the absence of the misfit. The thickness of the embedded layer is 1.1 times the critical thickness.

Fig. 18 Non-dimensional values of the nodal driving force G_i for the center node ($x_3' = 0$) and the interfacial node ($x_3'/b = h_p/2$) as a function of nodal position. The dotted curves correspond to the driving force in the absence of the blocking misfit. The threading dislocation was started at $x_2 = -300b$.

Fig. 19 Non-dimensional values of the nodal driving force G_i for the center node ($x_3' = 0$) and the interfacial node ($x_3'/b = h_p/2$) as a function of nodal position. The dotted curves correspond to the driving force in the absence of the blocking misfit. The threading dislocation was started at $x_2 = -600b$.

Fig. 20 The motion in the x_2, x_3'-plane of a threading dislocation that was started at $x_2 = -300b$. A misfit dislocation is positioned at $x_2 = 0$ and $x_3' = h/2\cos\alpha$. The thickness of the embedded layer is two times the critical thickness.

Fig. 21 Non-dimensional values of the nodal driving force G_i for the center node ($x_3' = 0$), an intermediate node ($x_3'/b = 3h_p/8$), and the interfacial node ($x_3'/b = h_p/2$) as a function of nodal position. The dotted curves correspond to the driving force in the absence of the blocking misfit. The threading dislocation was started at $x_2 = -300b$.

Fig. 22 Geometry for a segment C_{i+1} interacting with a second disjoint segment C_{m+1}.

Fig. 23 Geometry for a segment C_i interacting with a second disjoint segment C_{m+1}.

Fig. 24 Geometry for a segment C_{i+1} interacting with a second adjacent segment C_i.

Fig. 25 Geometry for a segment C_{i+1} interacting with two semi-infinite segments $y_1'y_2'$ and $y_1''y_2''$

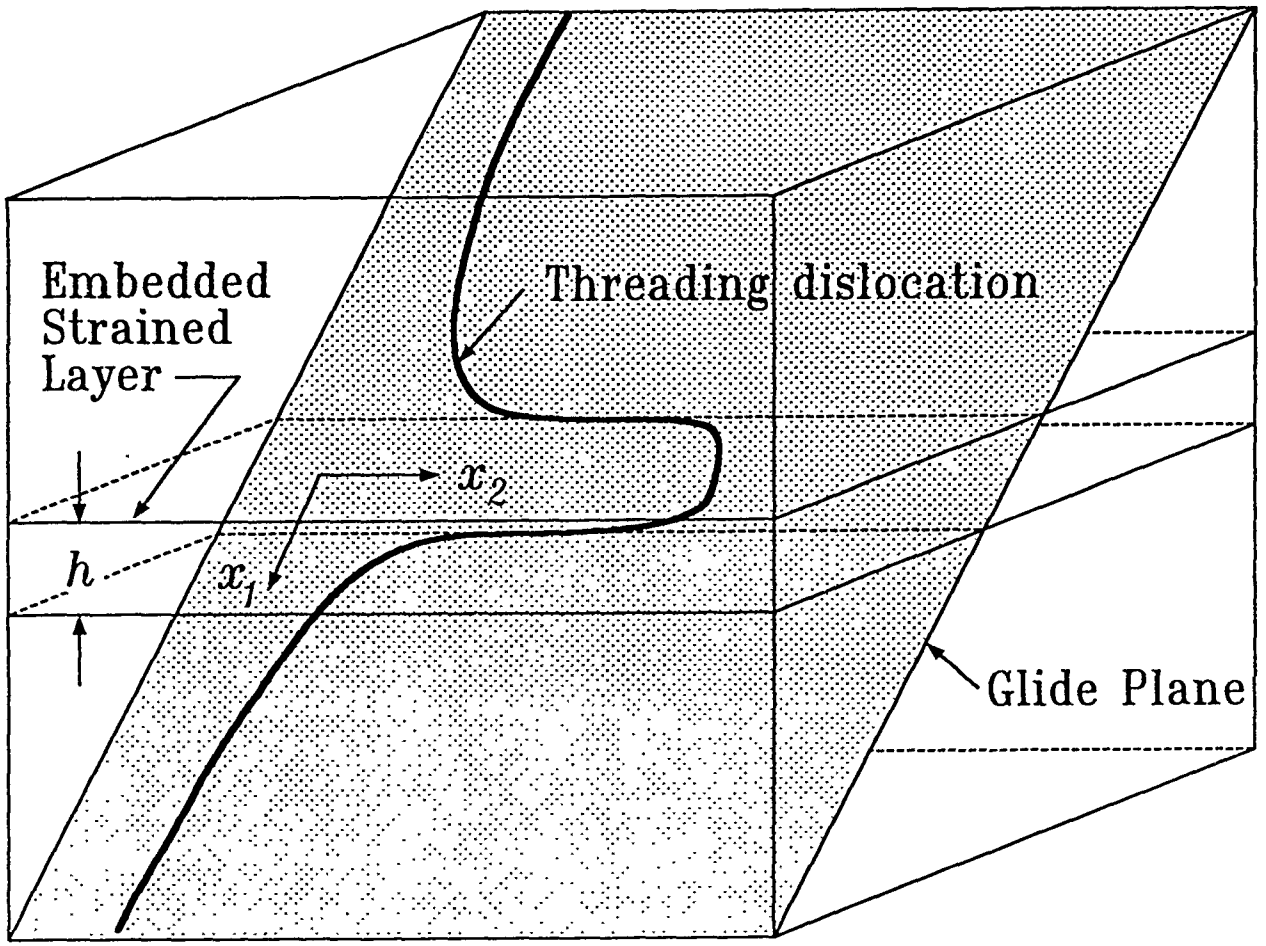
Embedded
Strained
Layer
Threading dislocation
x_2
h
x_1
Glide Plane

Figure 1

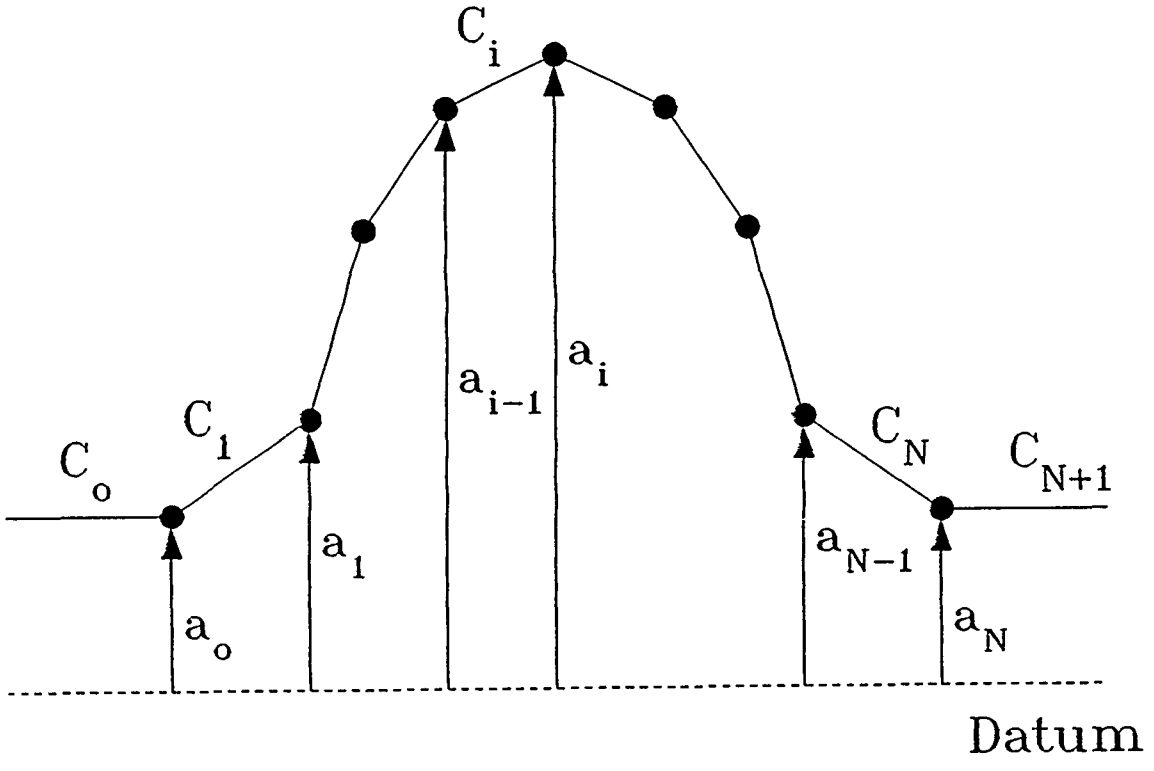

Figure 2

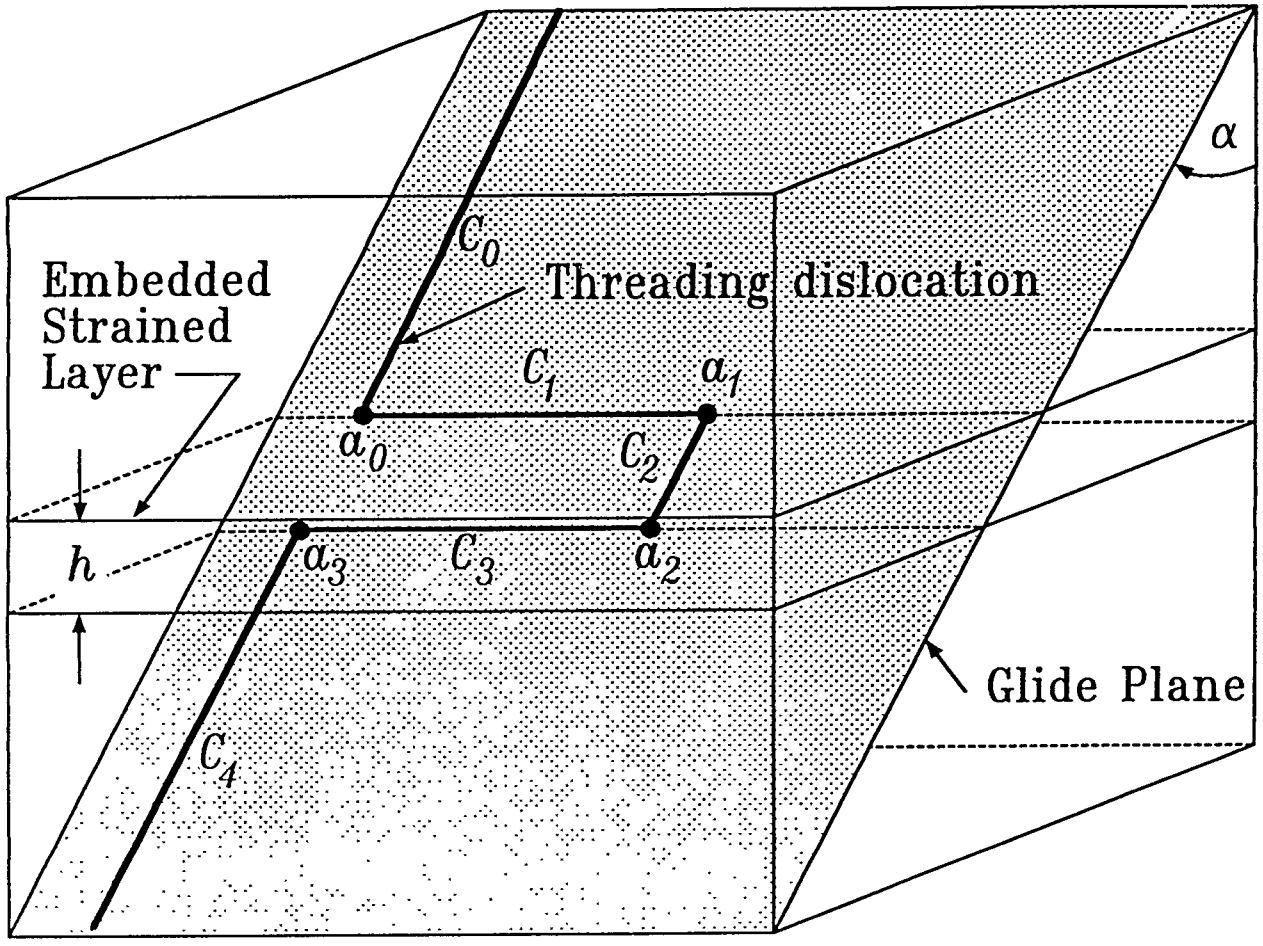
Embedded
Strained
Layer
h
C_0
Threading dislocation
C_1
a_1
a_0
C_2
a_3
C_3
a_2
C_4
α
Glide Plane

Figure 3

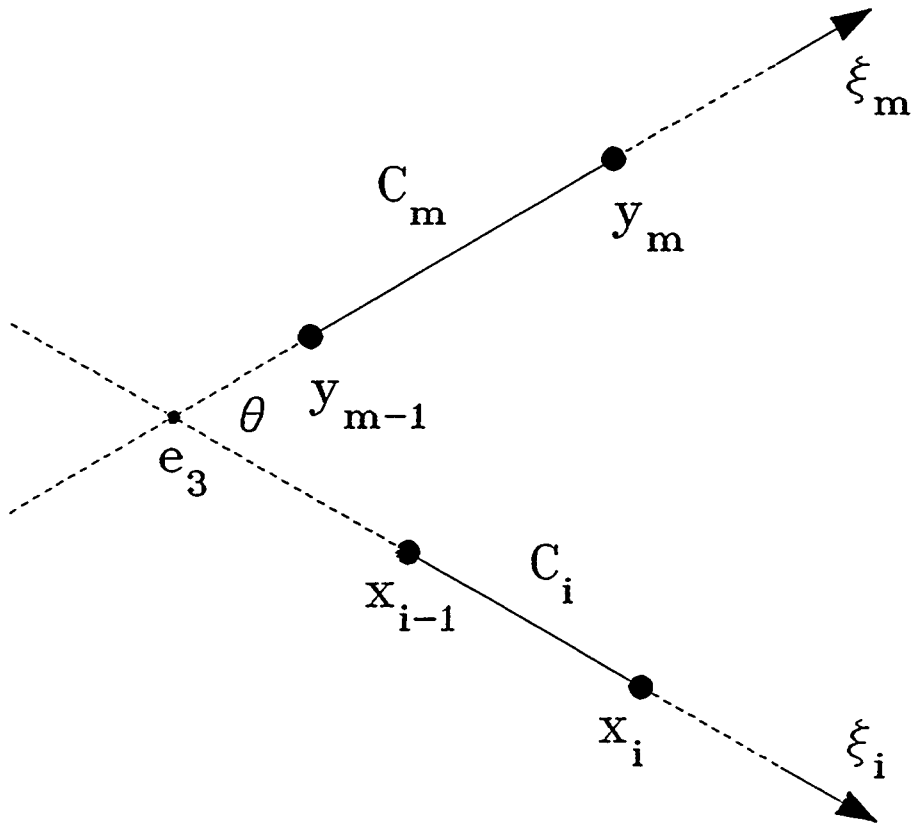

Figure 4

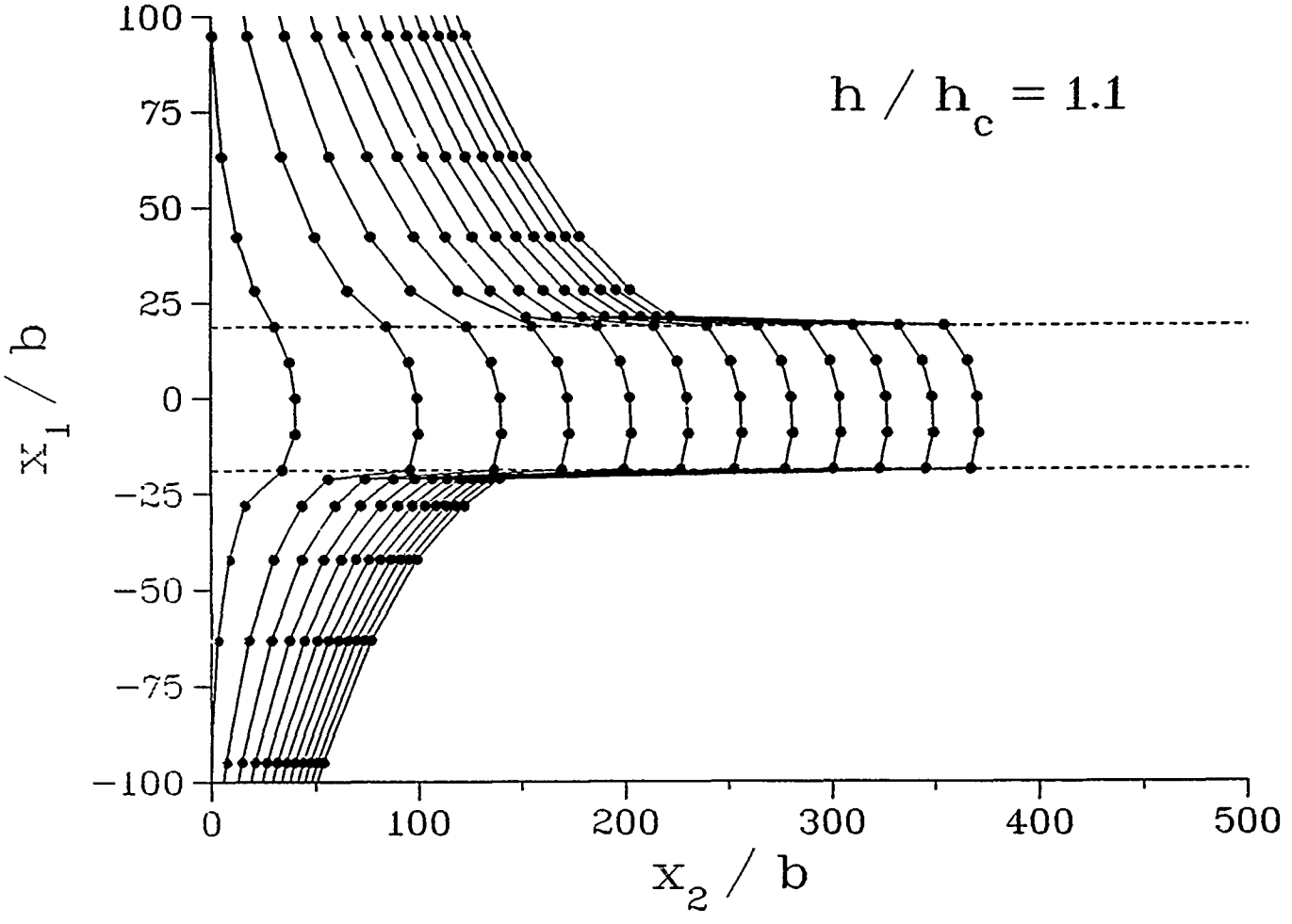

Figure 5

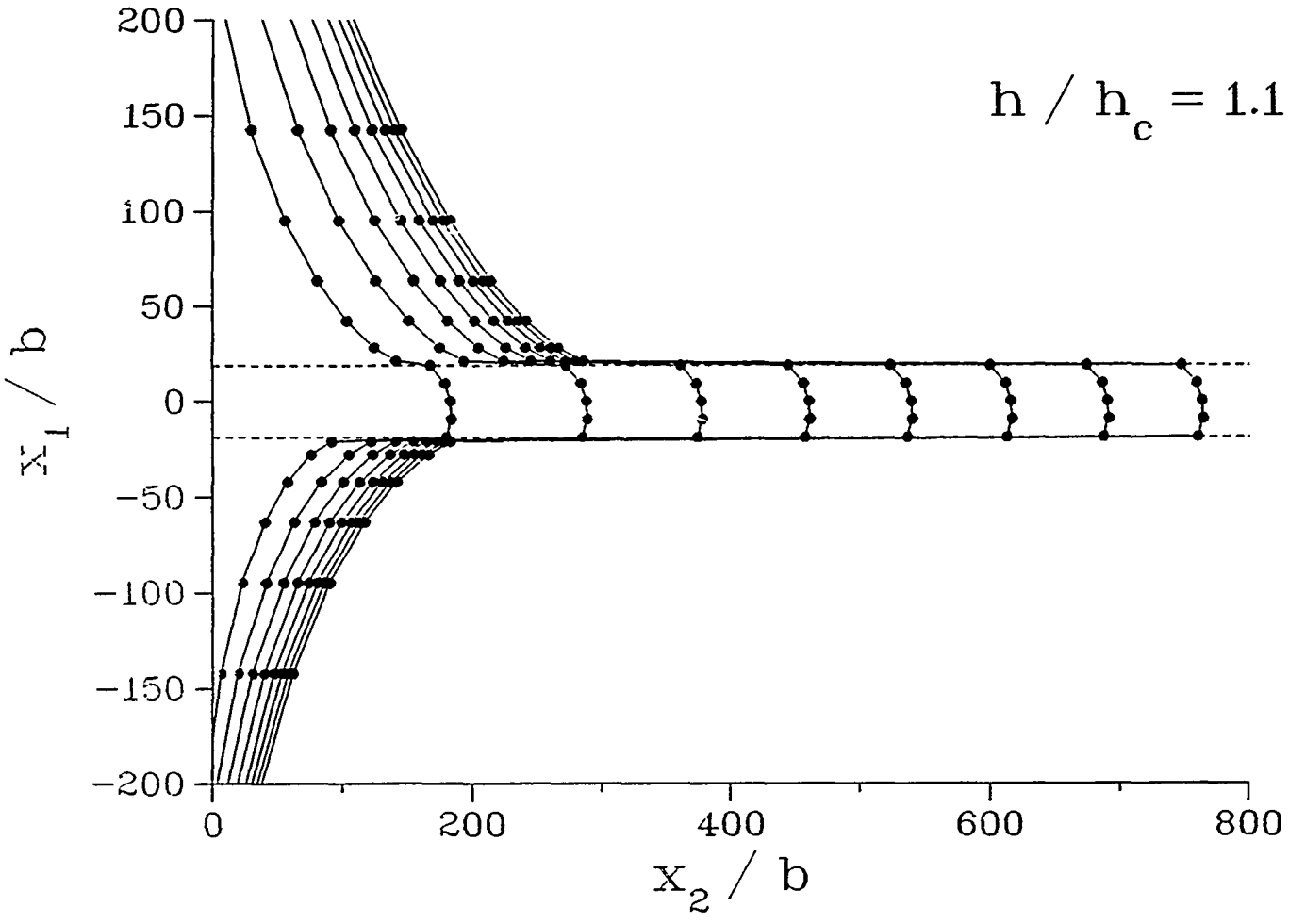

Figure 6

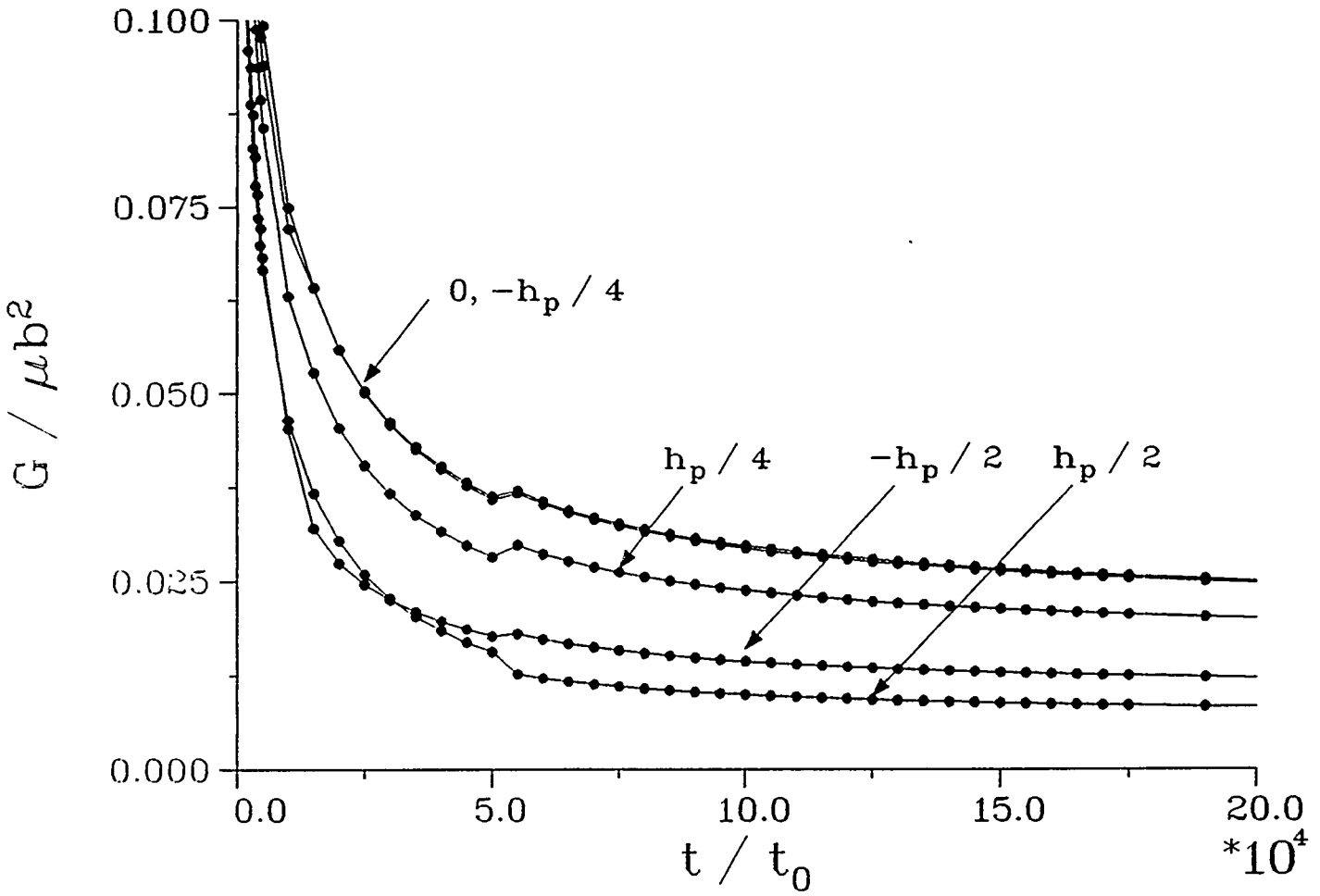
0.100
0.075
0.050
0.025
0.000
G / μb²
0, −h_p / 4
h_p / 4
−h_p / 2
h_p / 2
0.0
5.0
10.0
15.0
20.0
t / t_0
*10^4

Figure 7

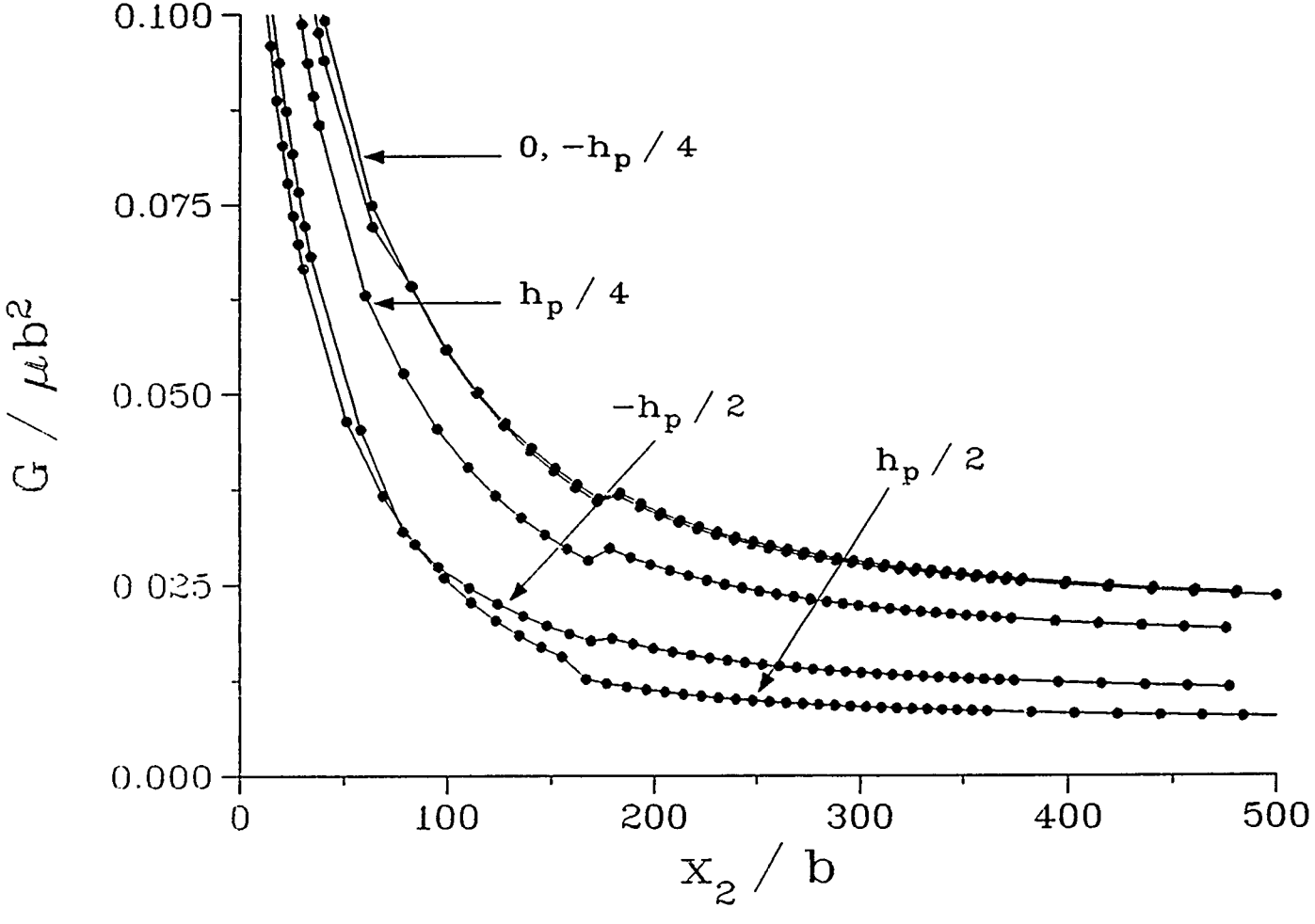
0.100
0.075
0.050
0 025
0.000
G / μb²
0
100
200
300
400
500
x₂ / b
0, −h_p / 4
h_p / 4
−h_p / 2
h_p / 2

Figure 8

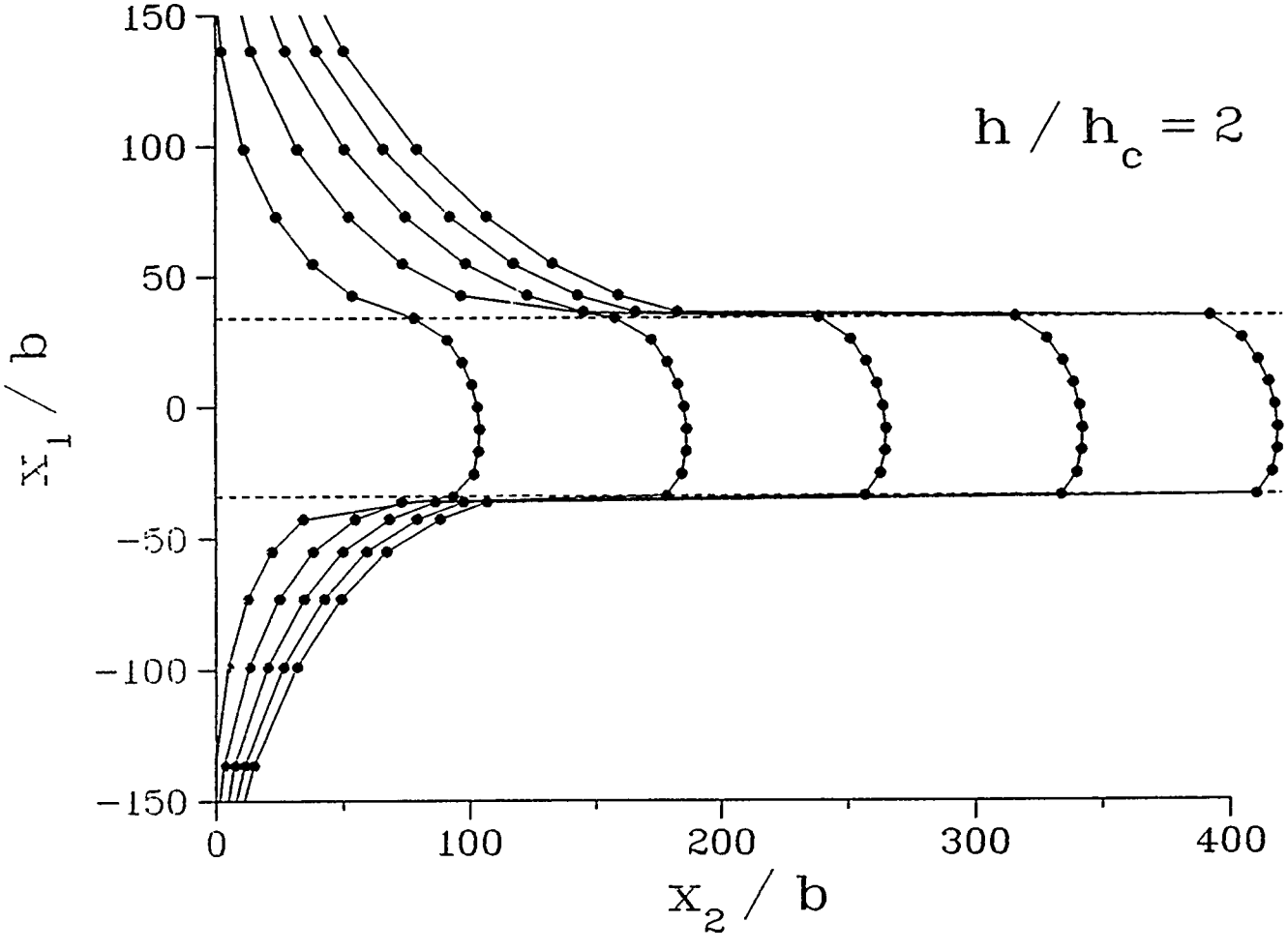

Figure 9

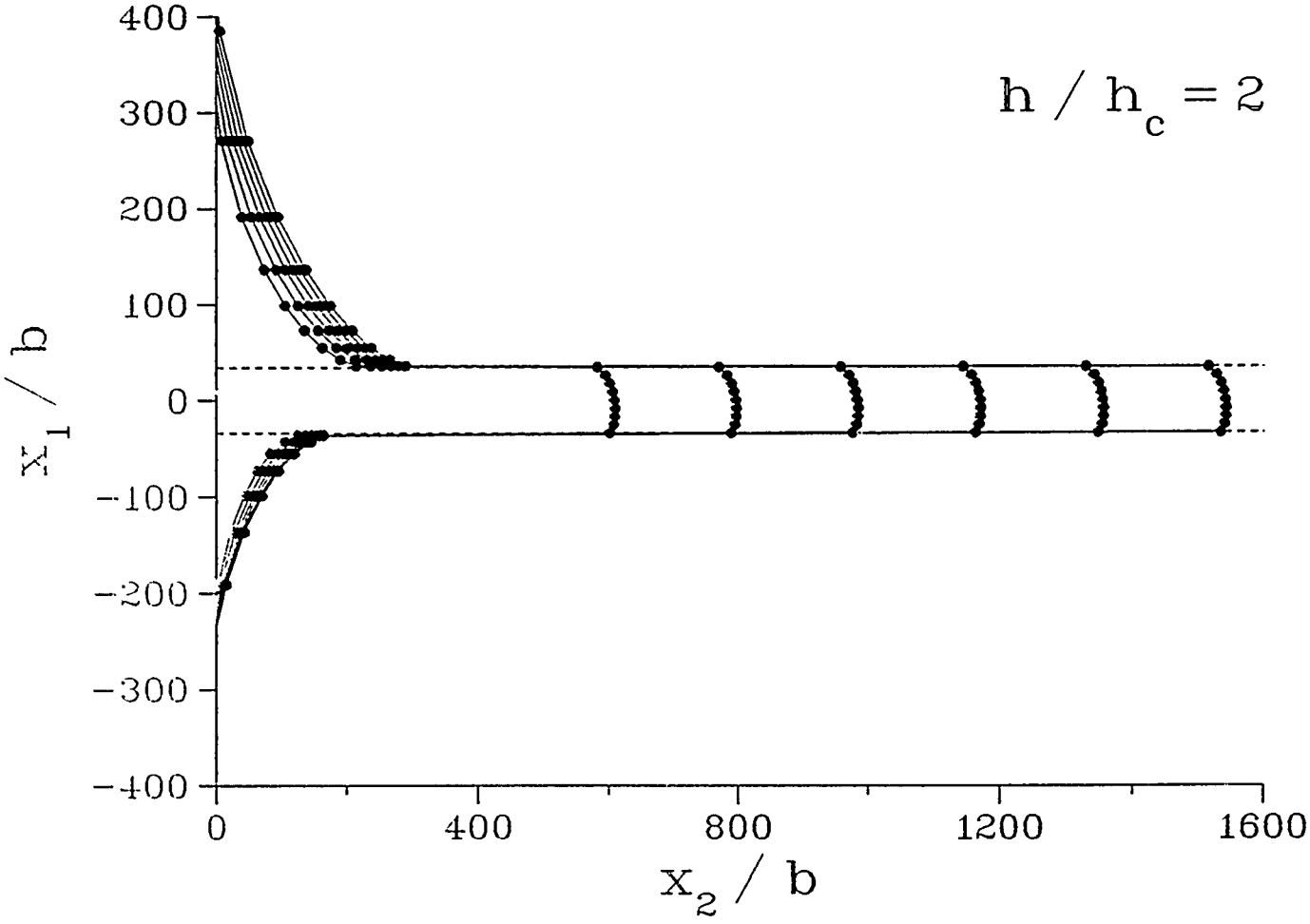
h / h_c = 2
400
300
200
100
0
-100
-200
-300
-400
x_1 / b
0
400
800
1200
1600
x_2 / b

Figure 10

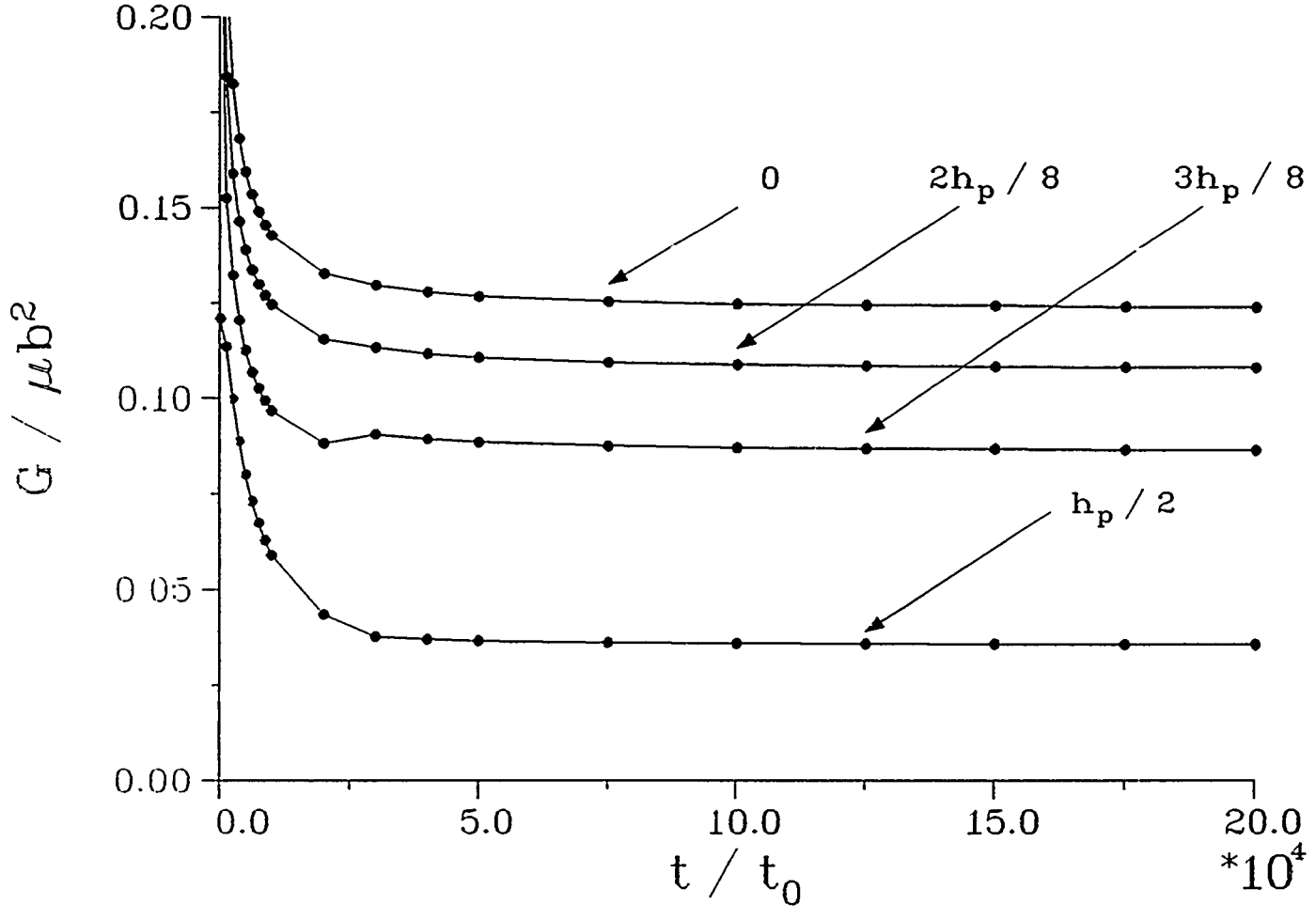
0.20
0.15
0.10
0 05
0.00
G / μb2
0
2hp / 8
3hp / 8
hp / 2
0.0
5.0
10.0
15.0
20.0
t / t0
*10^4

Figure 11

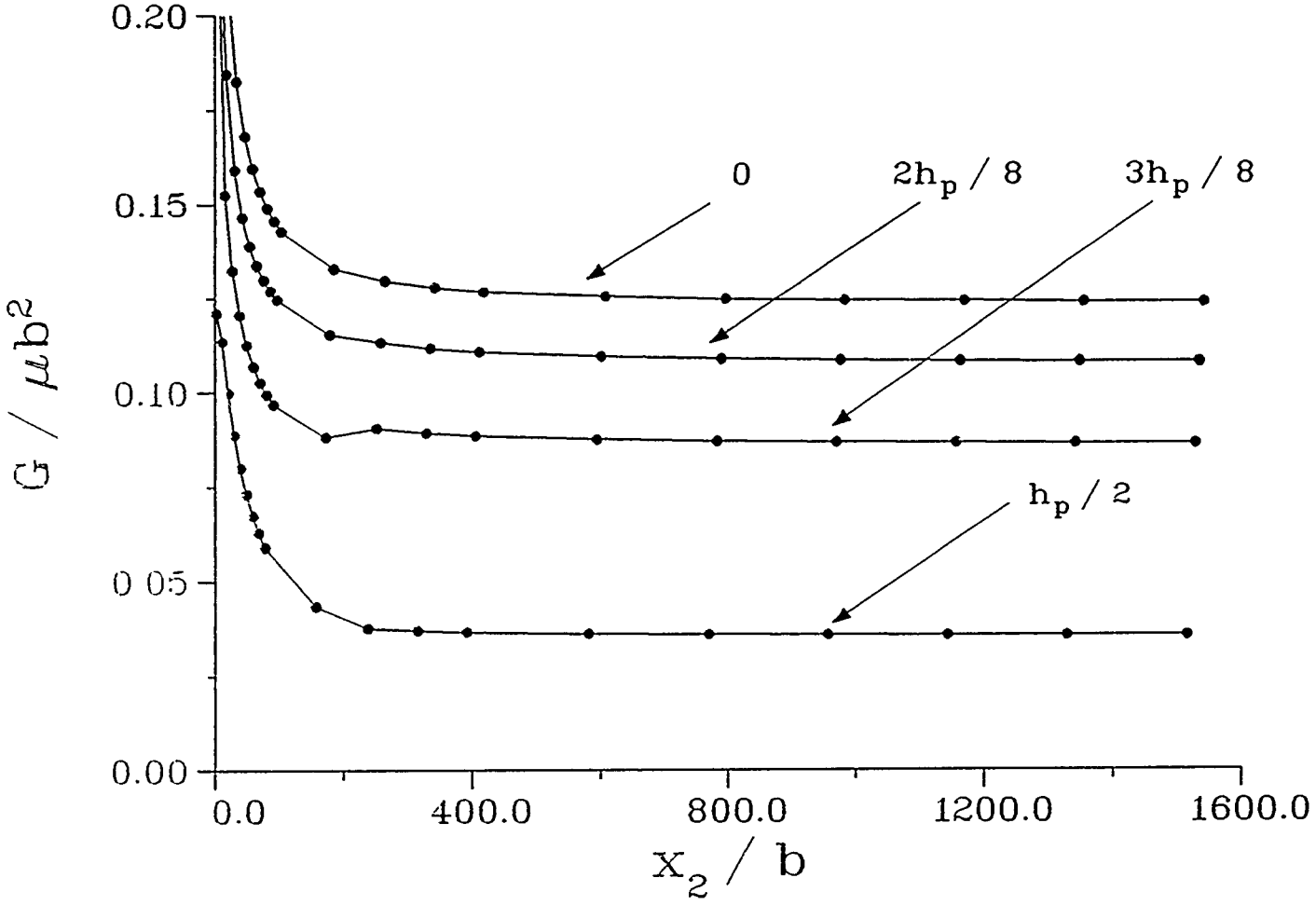
0.20
0.15
0.10
0 05
0.00
G / μb²
0
2h_p / 8
3h_p / 8
h_p / 2
0.0
400.0
800.0
1200.0
1600.0
x_2 / b

Figure 12

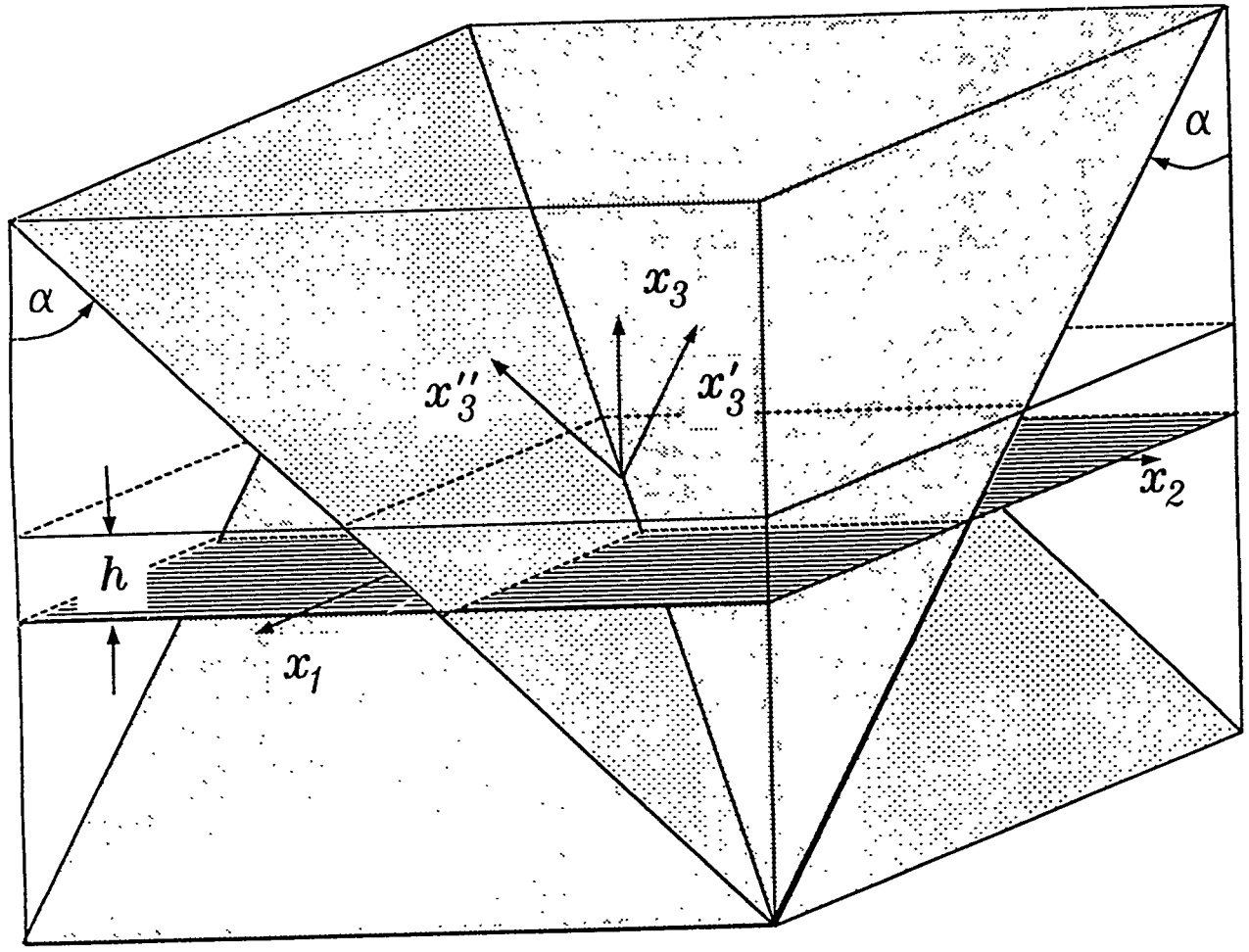

Figure 13

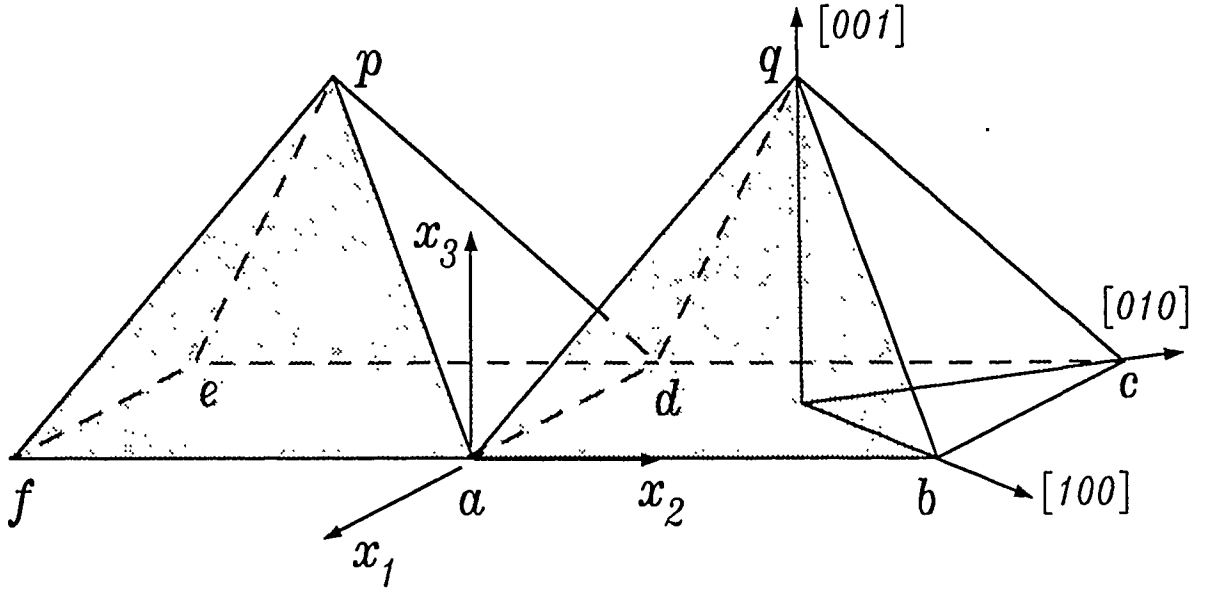

Figure 14

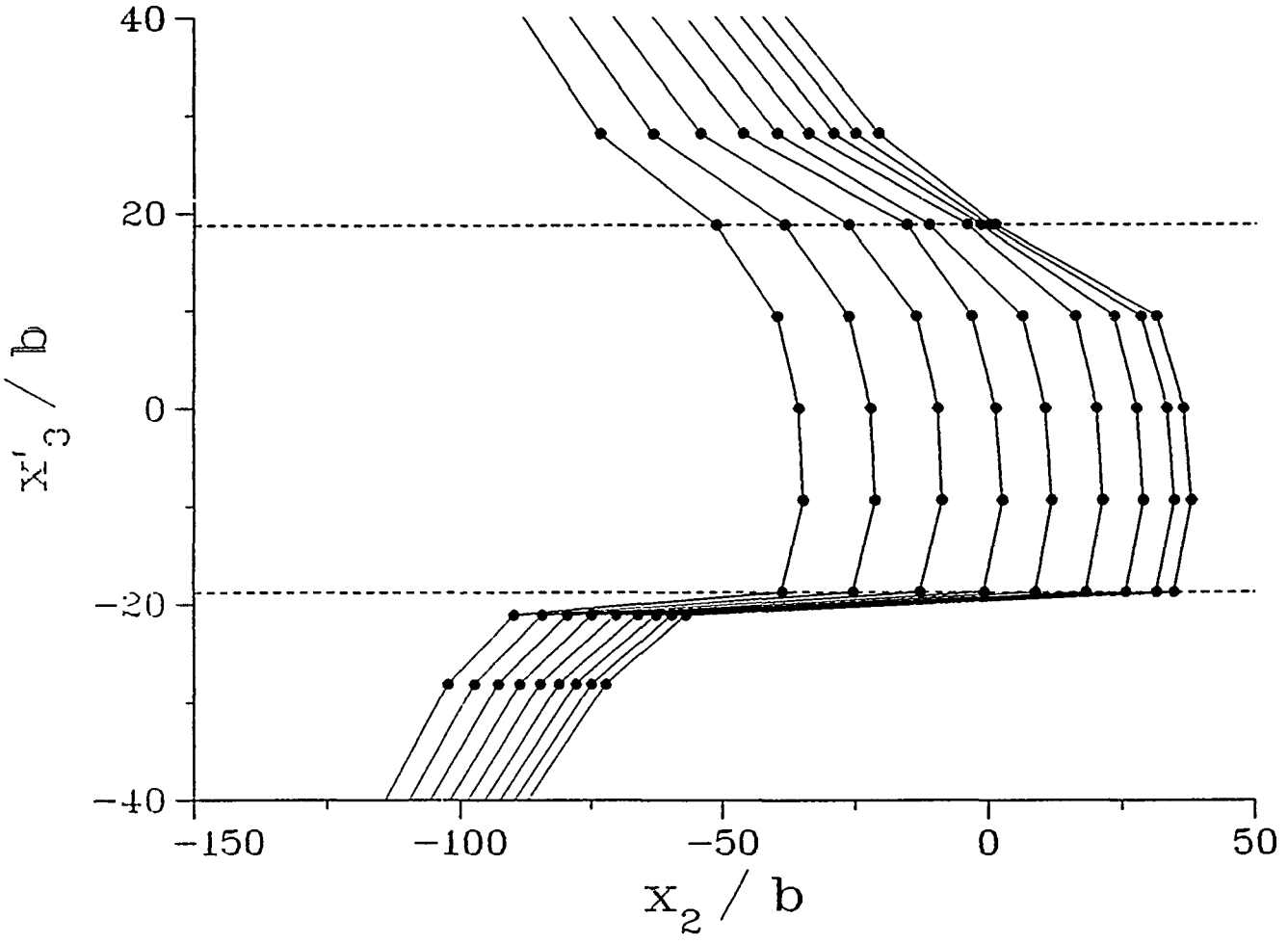

Figure 15

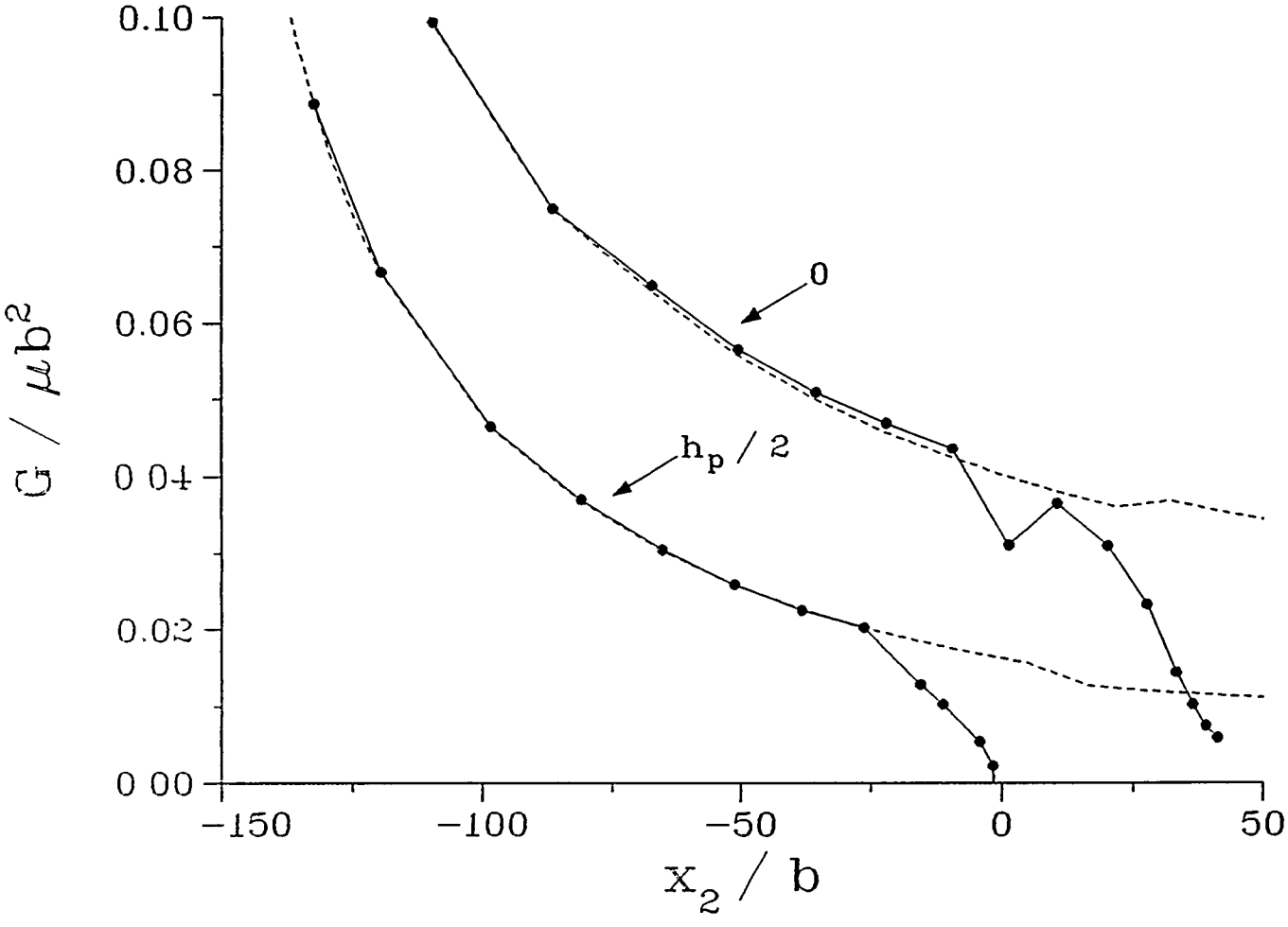

Figure 16

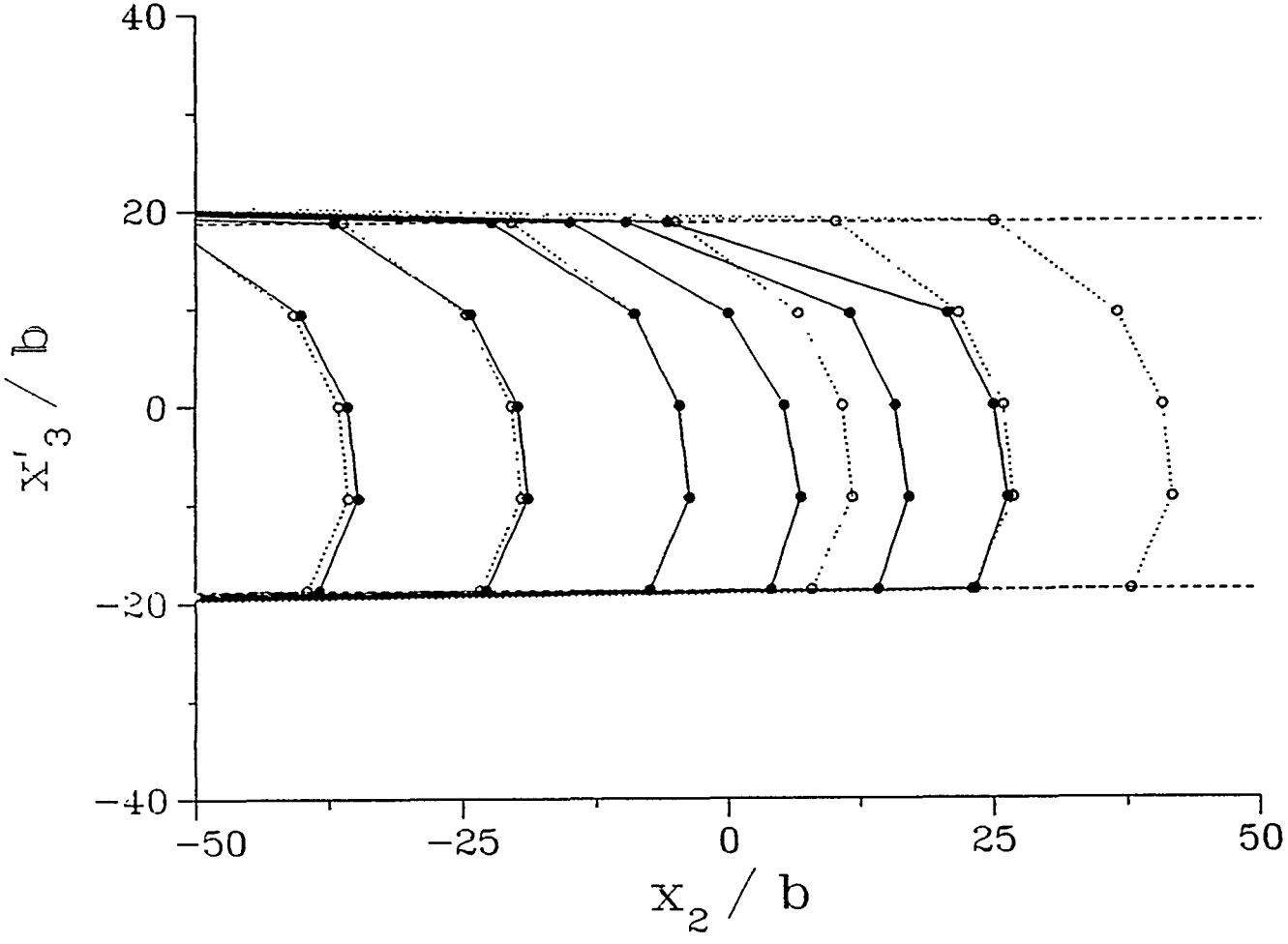

Figure 17

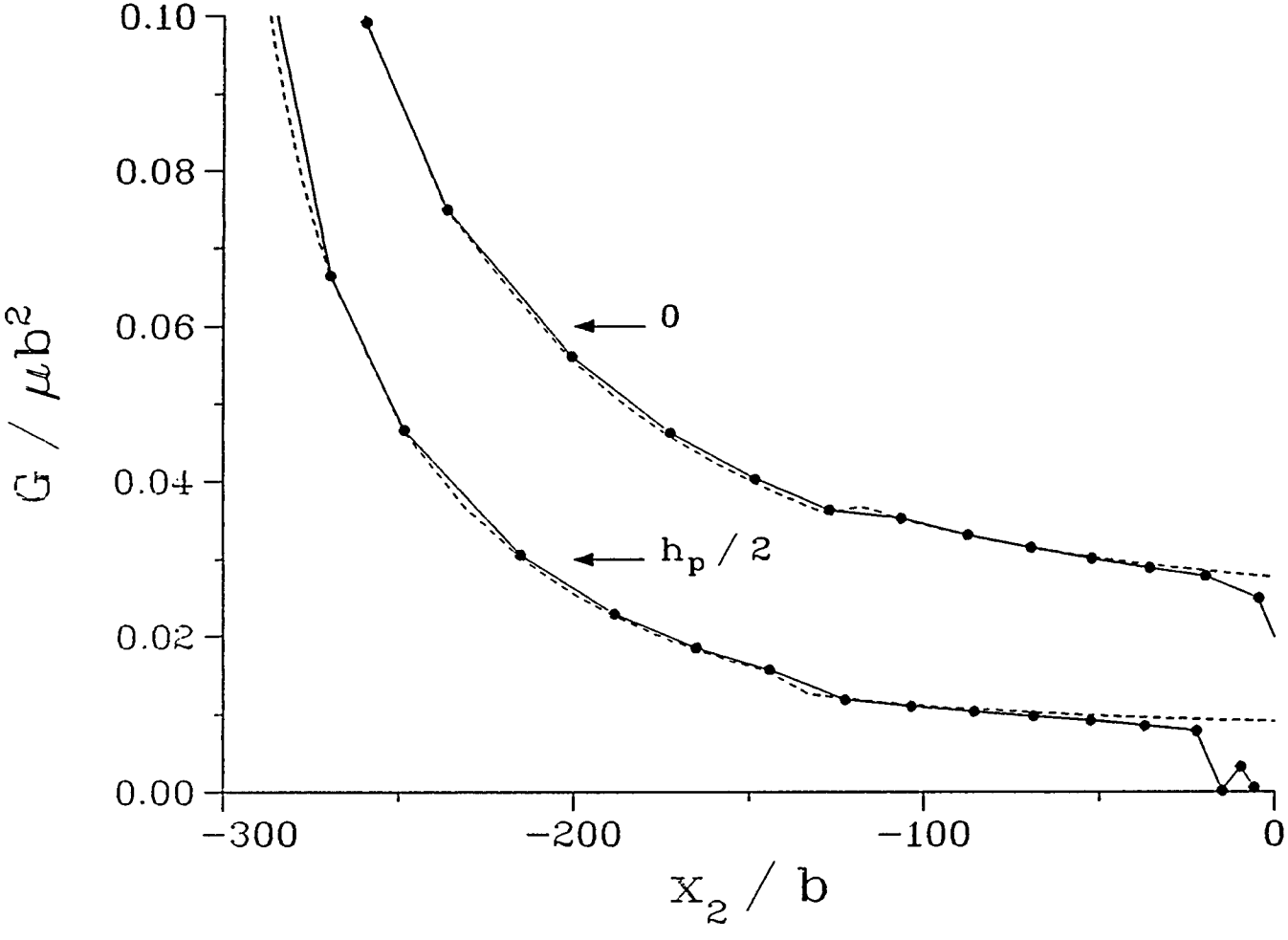

Figure 18

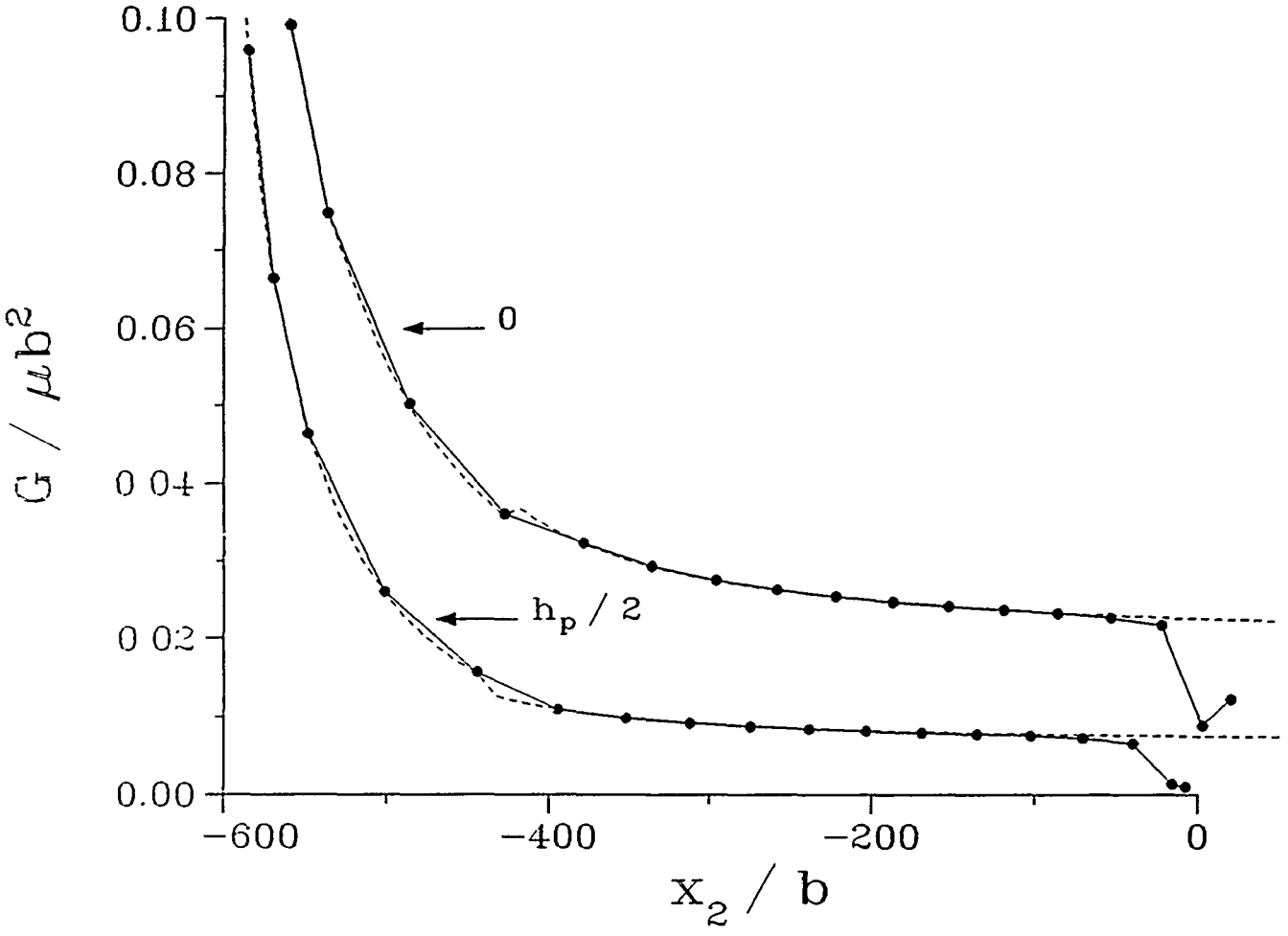

Figure 19

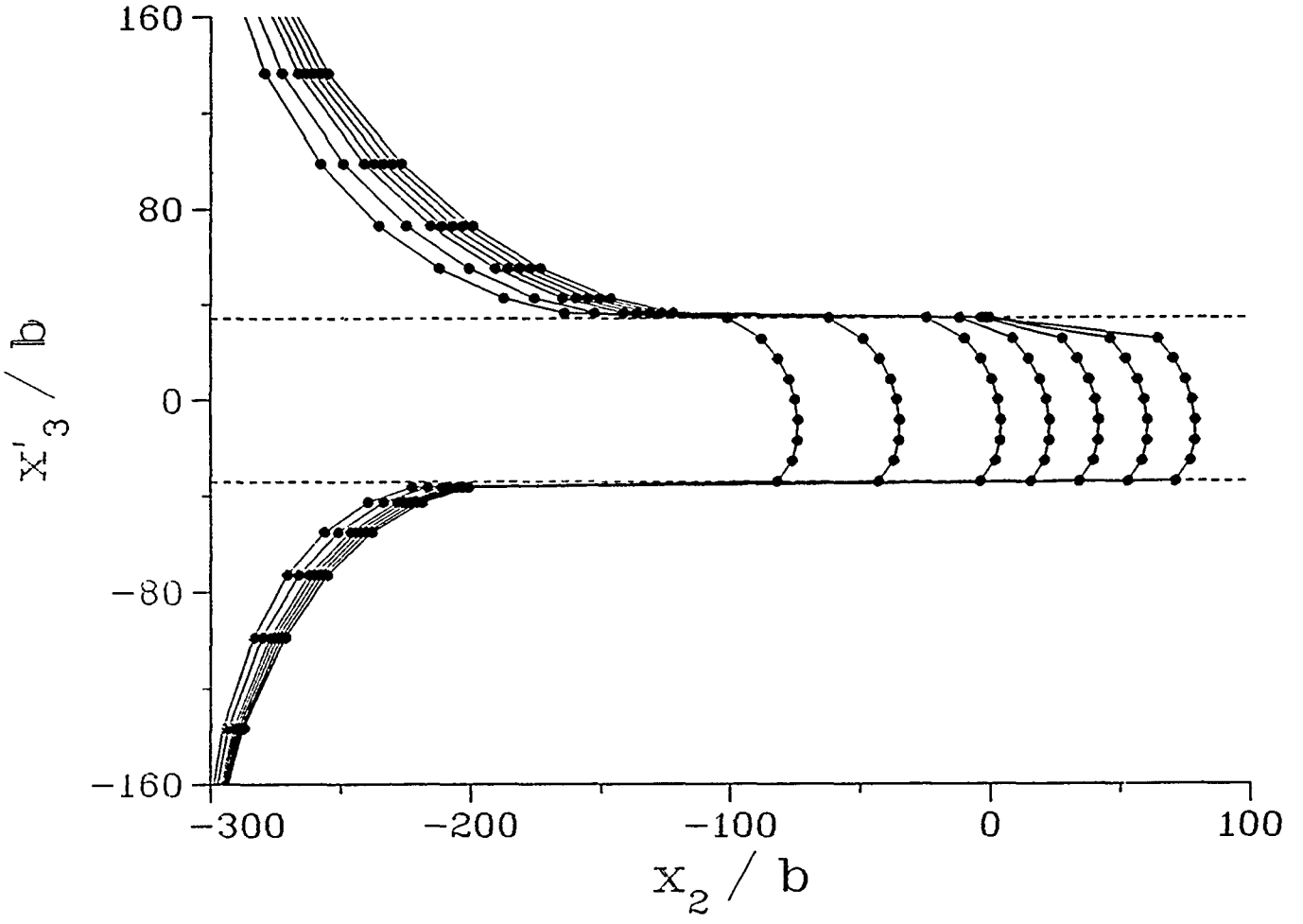

Figure 20

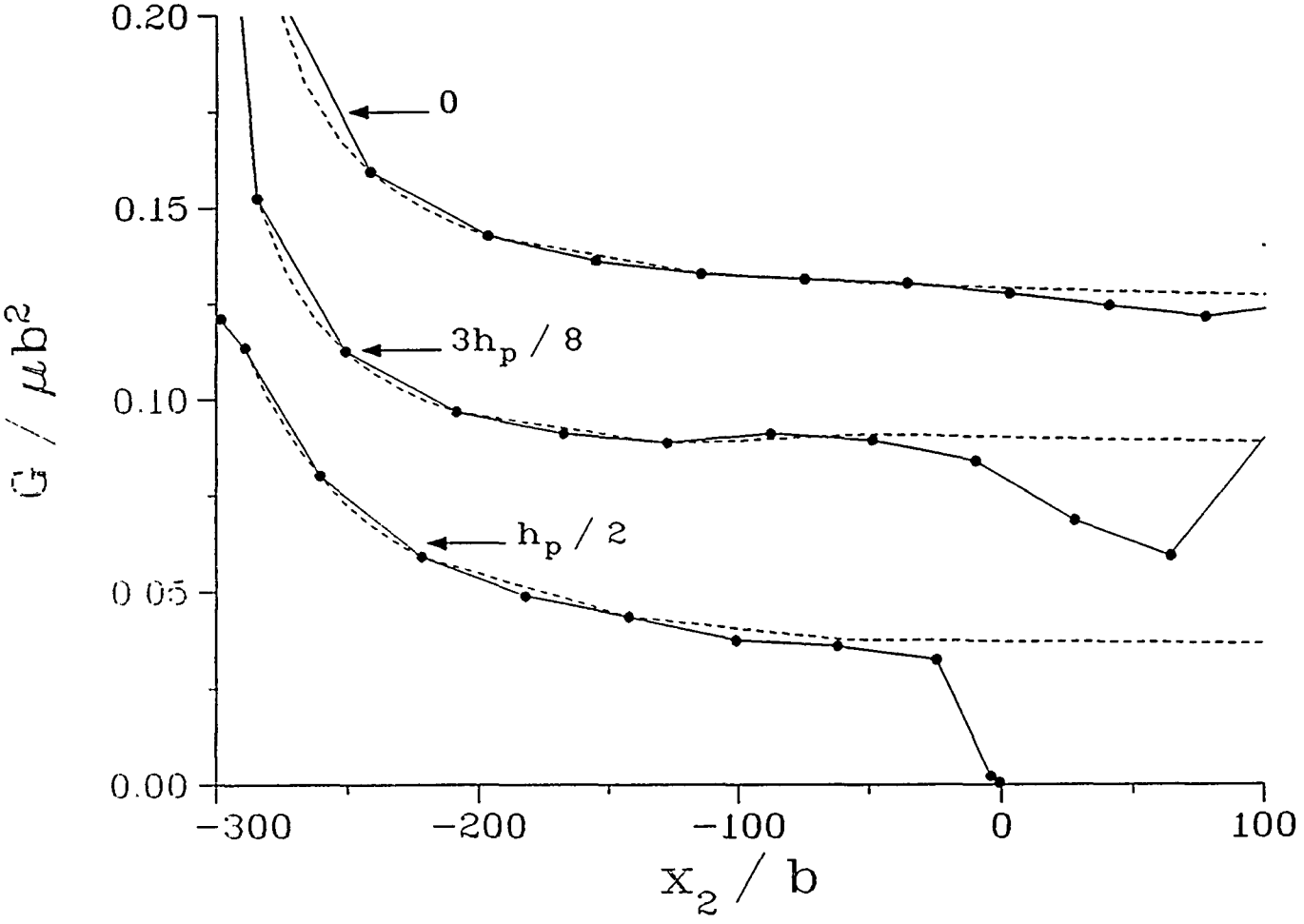

Figure 21

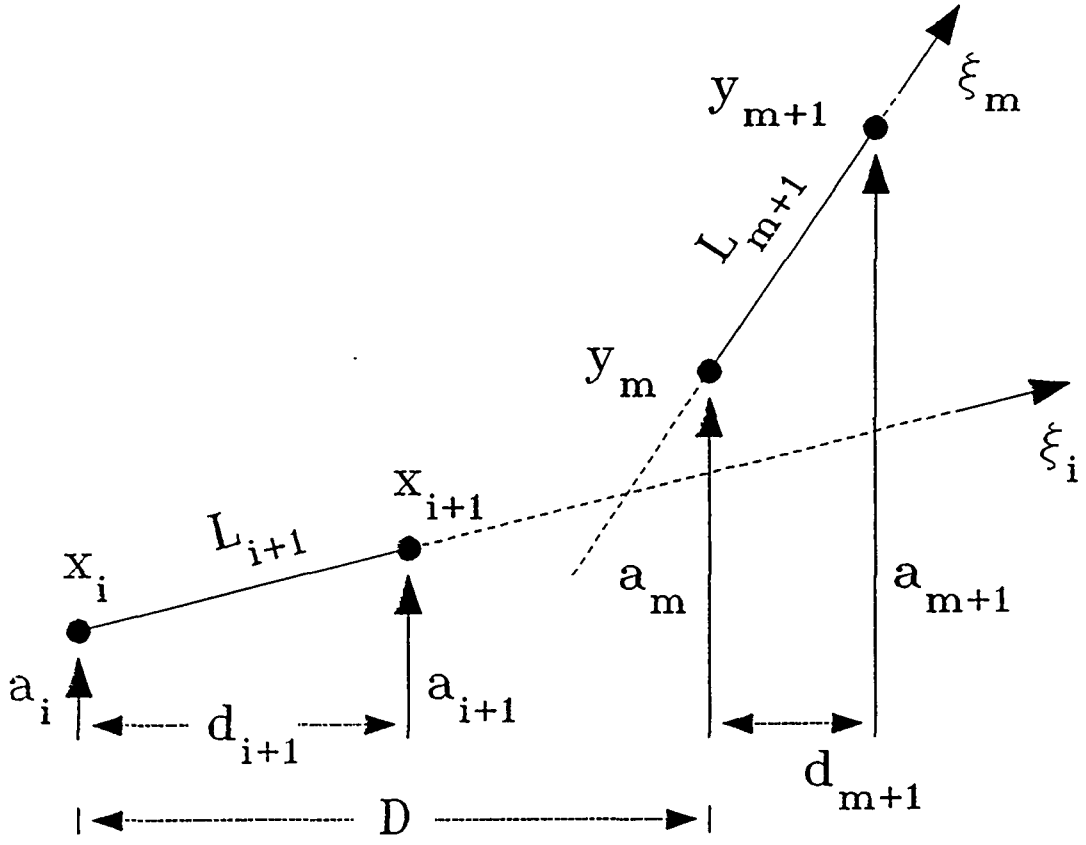

Figure 22

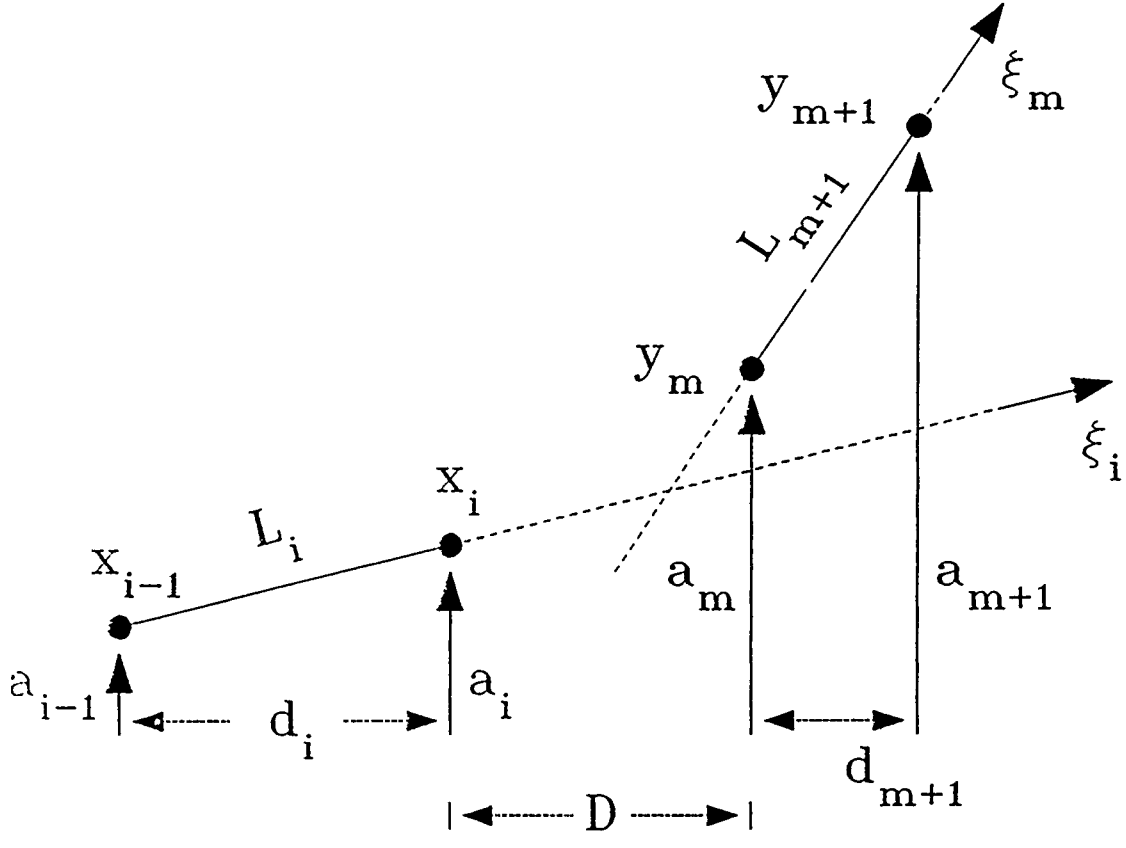

Figure 23

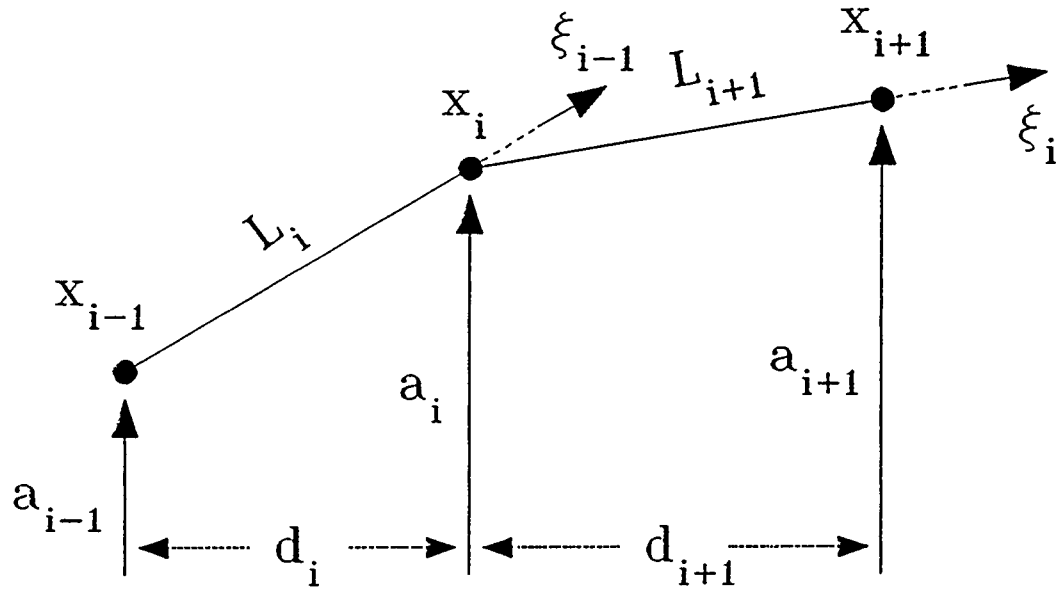

Figure 24

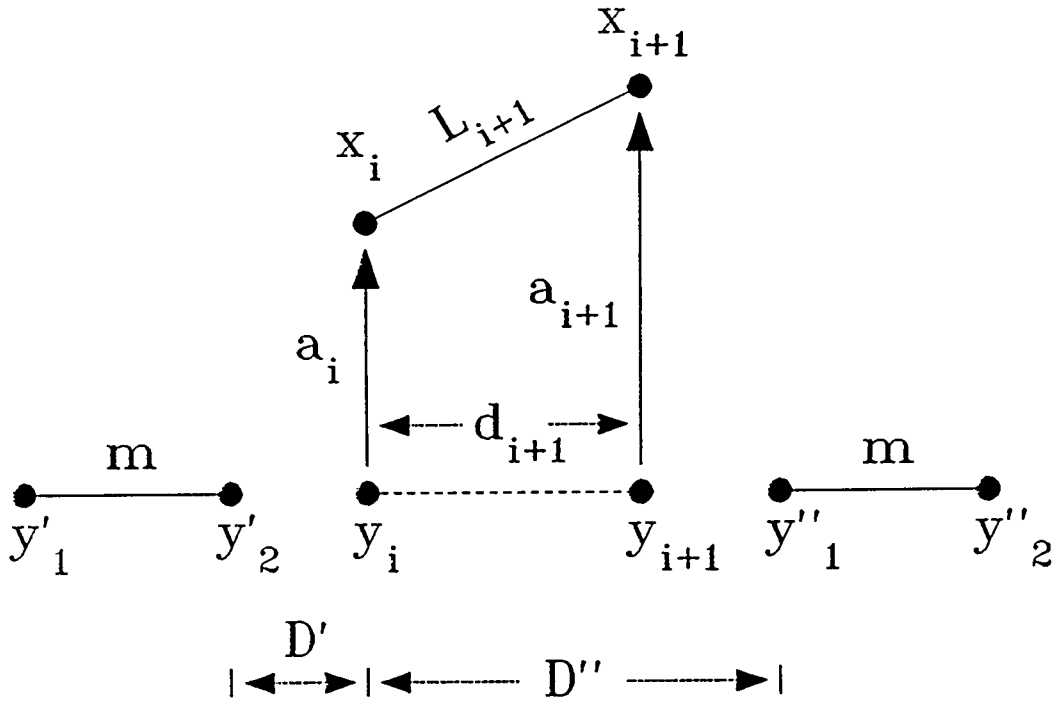

Figure 25